



# 6

## *The EUV PS/PDI — Schwarzschild Objective Testing*

---

<b>6.1 INTRODUCTION</b>	<b>106</b>
<b>6.2 EXPERIMENTAL COMPONENTS</b>	<b>106</b>
6.2.1 The 10× Schwarzschild Objective	
6.2.2 ALS Undulator Beamline 12.0	
6.2.3 <i>Hector's Magic Flange</i>	
6.2.4 Other Stages and Components	
6.2.5 Pinhole Spatial Filters	
6.2.6 High-Vacuum-Compatible High-Speed Shutters	
6.2.7 Beam Detectors	
<b>6.3 THE TEST WAVE</b>	<b>118</b>
6.3.1 Blemishes	
6.3.2 Illuminating Beam: <i>In Situ</i> Pinhole Size Assessment	
<b>6.4 THE REFERENCE WAVE</b>	<b>121</b>
6.4.1 The PS/PDI Reference Wave	
6.4.2 <i>In Situ</i> Pinhole Size Assessment	
<b>6.5 FOURIER-TRANSFORM ALIGNMENT METHOD</b>	<b>124</b>

## 6.1 INTRODUCTION

The EUV PS/PDI was developed for at-wavelength measurement of lithographic-quality reflective optical systems operating near 13-nm wavelength and 0.1 NA. This chapter describes procedures and results of a wide range of experiments intended to study the properties of the Schwarzschild objective, the interferometer, and the testing methods themselves.

Using a specially-designed undulator beamline at the Advanced Light Source at Ernest Orlando Lawrence Berkeley National Laboratory, successful characterization of a multilayer-coated 10 $\times$ -demagnification Schwarzschild objective was conducted between November 1996 and May 1997. These experiments include intensity and wavefront measurements of the three off-axis sub-apertures, investigation of the spatial filtering properties of the pinholes and windows used in the interferometer, studies of the mechanical properties of the interferometer system, and analysis of wavelength-dependent *chromatic aberrations* arising from the resonant-reflective multilayer coatings. Extensive tests were also performed to evaluate the measurement methods and their precision.

EUV PS/PDI interferometry demonstrated angstrom-range wavefront-measuring precision and sub-nanometer measurement accuracy. Repeated measurements conducted over a span of several weeks show a high degree of system stability and repeatability, yet careful investigations of the experimental data have enabled the identification of areas in which further improvements can be made. As of Fall 1997, the EUV PS/PDI experiments are still in progress. These ongoing experiments seek to push the measurement accuracy to new limits.

It was known in advance that the EUV PS/PDI system is best designed for the measurement of nearly diffraction-limited optical systems. When systems contain large wavefront aberrations or mid-spatial-frequency defects, accurate measurement becomes very challenging. From the three off-axis sub-apertures that were measured, a wide range of experimental conditions were encountered. Experiences and insights are discussed in this chapter.

## 6.2 EXPERIMENTAL COMPONENTS

Many of the components used in the PS/PDI experiments are the same as or are similar to those used in the earlier PDI experiments. A newer, dedicated beamline source is optimized for high flux and moderate bandwidth. Yet the same 8-cm-period undulator and optical table used in the EUV Fresnel zone-plate measurements are still in use. The CCD detector used to record the interference patterns is also of the same specifications as before. In this section, several of the most important components of the experiment are described in detail.

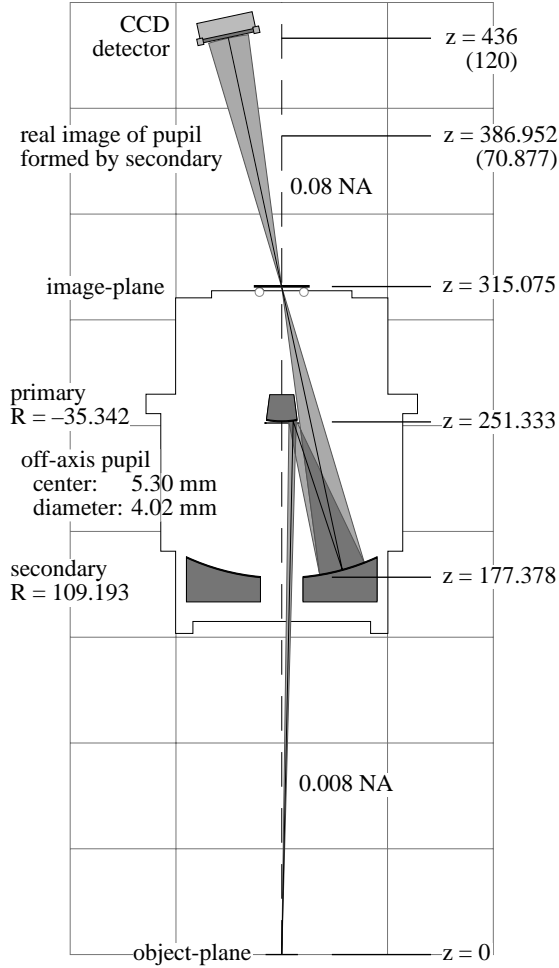


**Figure 1.** Optical design of the 10× Schwarzschild objective, shown to scale and in the proper orientation: light is incident vertically from the bottom. The primary and secondary mirror substrates are shown in gray. All units are in mm.

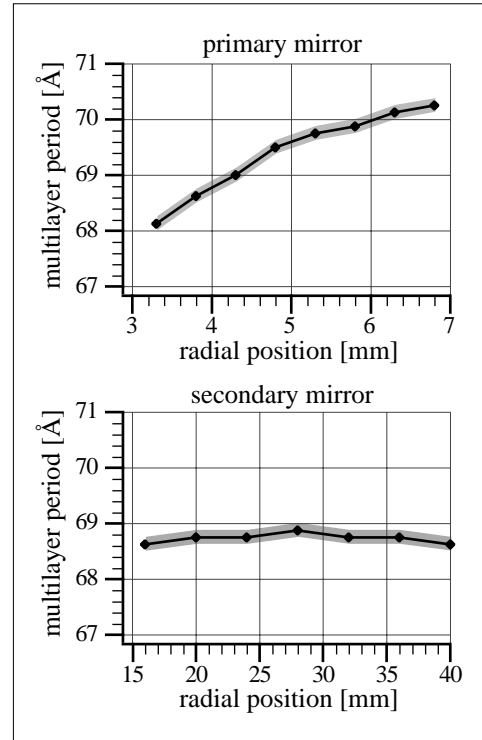


**Figure 2.** The measured period of the Mo/Si multilayer coatings of the 10× Schwarzschild objective. The primary mirror is designed with a graded coating to compensate for the large range of incident angles. The measurement uncertainty of 0.125 Å is indicated as a gray band about the measured points.

### 6.2.1 The 10× Schwarzschild Objective

The 10× Schwarzschild objective studied in these experiments is one of four Schwarzschild optics created to the same optical design specifications (Tichenor et al. 1993, 1994a; Kubiak et al. 1994, Bjorkholm et al. 1995, Wood et al. 1997). This particular optic is referred to as “10×B” (Berkeley) to distinguish it from two similar optics, 10×I and 10×II, which are used in prototype micro-stepper EUV imaging applications at Sandia National Laboratory, in Livermore, California. The fourth optic is used at Brookhaven National Laboratory by researchers from AT&T Bell Laboratories, also for interferometric applications.

The optical design calls for two nested spherical mirror substrates, Mo/Si multilayer-coated and designed for peak reflectivity and optimized performance at 13.4-nm wavelength. The specifics of the optical design are shown in Fig. 1. The full optic has an annular pupil, yet only one off-axis sub-aperture

is illuminated at a time. The unobstructed object-side and image-side numerical apertures of 0.008 and 0.08, respectively, are defined by a removable aperture stop that rests against the primary mirror. The optic is designed to have a circular, 400- $\mu\text{m}$ -diameter field of view in the image-plane, with a 1- $\mu\text{m}$  depth-of-focus.

The multilayer-coating deposition and measurement were performed by David Windt. The large range of angles-of-incidence (13.1 to 29.1 mrad, or  $0.75^\circ$  to  $1.67^\circ$ ) across the convex primary mirror necessitated the deposition of a graded multilayer substrate to maintain high reflectivity and uniform phase across the radius of the aperture. The experimentally-measured graded thickness variation is shown in Fig. 2.

Visible-light interferometry was used to measure the individual mirror substrates, and a process of *clocking* (aligning the relative azimuthal rotational orientation of the two mirrors) was performed to achieve the minimum predicted wavefront error in one of the off-axis sub-apertures.

Not knowing in advance what the magnitude or type of the EUV wavefront aberrations would be, a strategy was adopted wherein the optic was given an entrance pupil with three apertures of different sizes as shown in Fig. 3. The removable aperture stop rests against the central point of the primary mirror and separately defines 0.06, 0.07 and 0.08 NA apertures. The 0.08 NA sub-aperture was accidentally broken during fabrication, creating the “D” shape. The circular apertures occupy a plane normal to the mechanical axis of the optic. The off-axis illumination encounters the circular pupil at an angle of  $1.2^\circ$  from the central ray to the vertical, making the pupil appear slightly foreshortened in the radial direction and therefore elliptical. Because of the reflection, the beam passes through the aperture twice.

The optic and its mechanical housing were designed to be used in the vertical orientation with the image-plane at the top of the mechanical housing. The image-plane is defined by three small, carefully chosen steel balls. In imaging applications, the wafer rests on these three balls with the photoresist facing downward. Because the optic is designed to be used in this vertical orientation, and any change of orientation could possibly introduce mechanical or gravitational changes to the mirror substrates, all EUV inter-

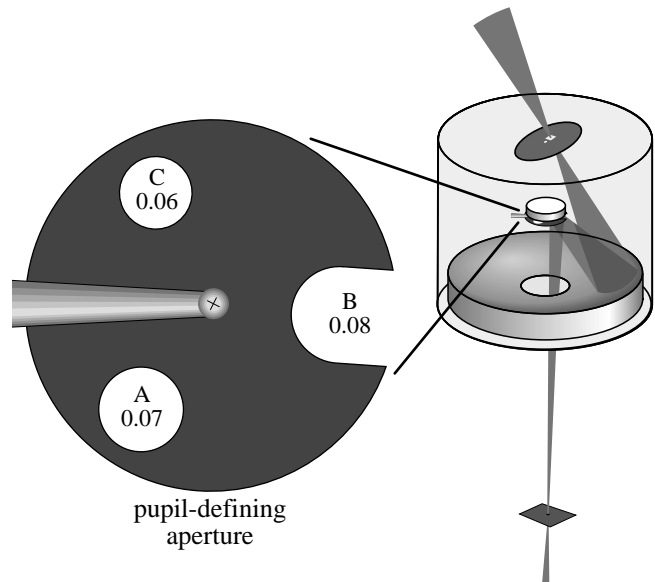


**Figure 3.** A removable aperture stop, placed against the primary mirror of the 10 $\times$  Schwarzschild objective, defines three sub-apertures with 0.08, 0.07, and 0.06 NA. The 0.08 NA aperture (broken during fabrication) is positioned above the region predicted to have the highest wavefront quality, based on visible-light interferometry. All three sub-apertures are investigated at EUV wavelengths.

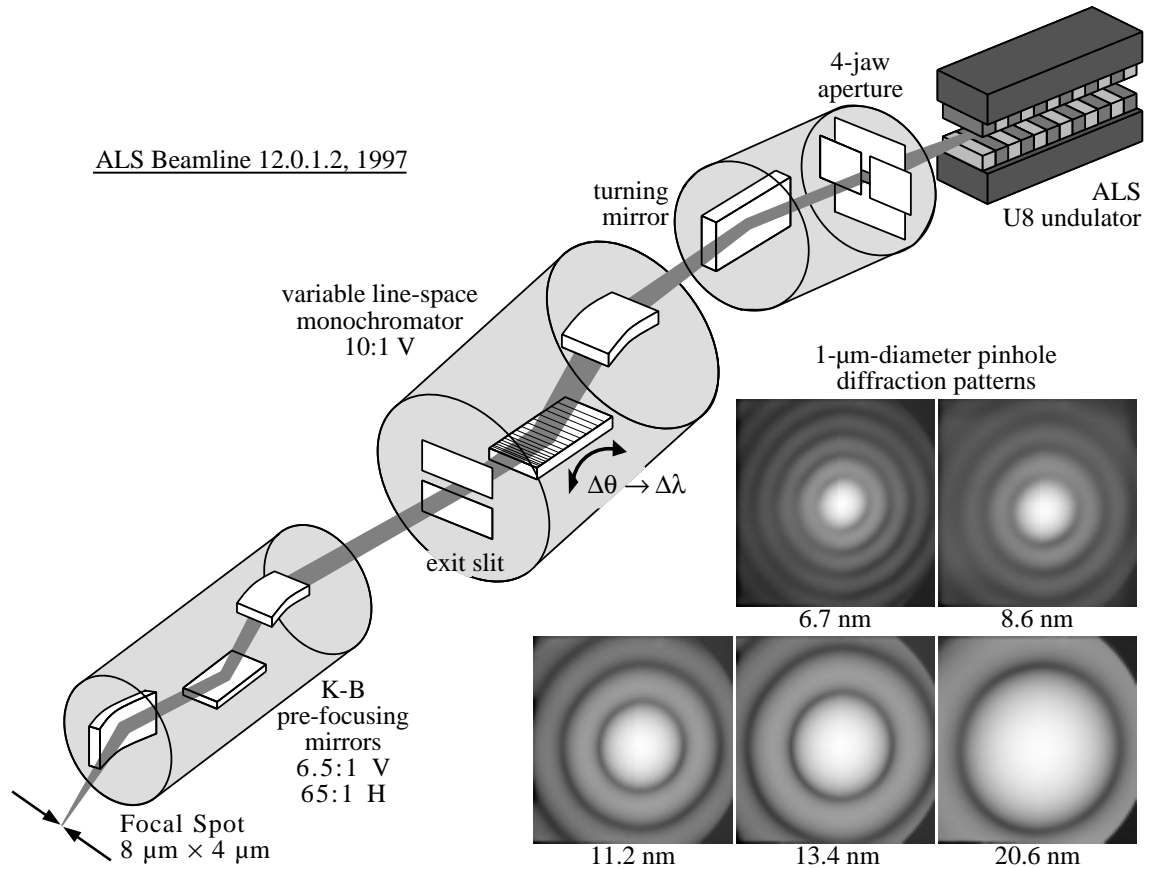


**Figure 4.** The key optical elements of ALS Undulator Beamline 12.0.1.2, a tunable, coherent EUV source, 1997. A four-jaw aperture and turning mirror select the EUV components of the narrow central cone of the undulator radiation. A variable-line-space planar-grating monochromator incorporating a vertical focusing mirror produces a resolution of  $\lambda/\Delta\lambda = 200\text{--}1000$ . The Kirkpatrick-Baez (K-B) mirror pair vertically images the monochromator exit slit and horizontally images the source onto the object-plane of the interferometer. The entire beamline produces a demagnification of 65 in both the horizontal and vertical directions. Measured pinhole diffraction patterns are shown for five EUV wavelengths, using a logarithmic grayscale. Only the central portion of the diffraction pattern is used as the illumination reference wavefront.

ferometric tests were performed vertically with the optic illuminated from below.

### 6.2.2 ALS Undulator Beamline 12.0

An undulator beamline, containing a grating monochromator followed by a Kirkpatrick-Baez (K-B) mirror pair, delivers radiation from the undulator to the interferometer (Attwood et al. 1993, Beguiristain et al. 1996). The beamline is shown schematically in Fig. 4. The angular demagnification of the beamline is designed to maximize the coherent flux available for illumination of the Schwarzschild objective near 13-nm wavelength. The entire system operates under vacuum, in pressures ranging from  $5 \times 10^{-11}$  torr in the beamline to  $5 \times 10^{-7}$  torr in the interferometer chamber.

In conjunction with the undulator, the monochromator allows the wavelength to be tuned continuously from 5 to 25 nm, with a spectral resolution in the range of  $\lambda/\Delta\lambda \sim 200\text{--}1000$ . The monochromator contains a planar blazed grating with variable line spacing, illuminated at glancing incidence. The exit slit

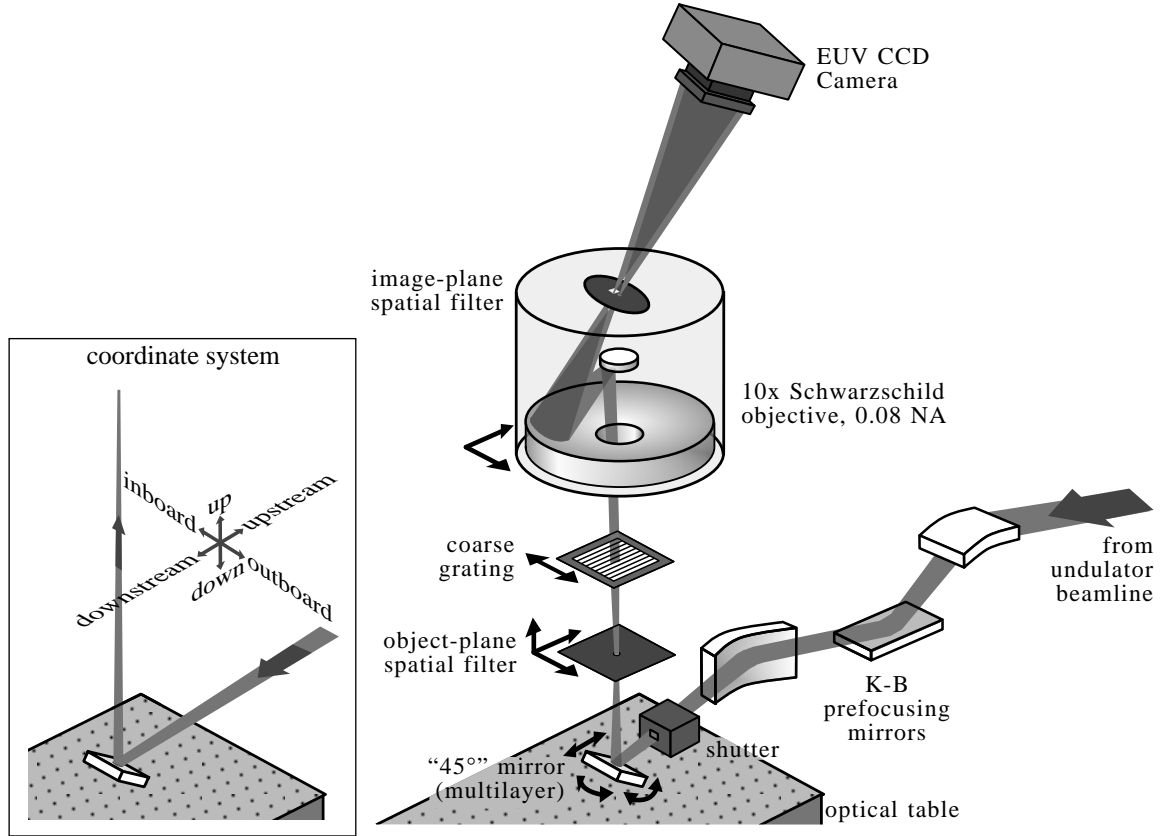


**Figure 5.** The key optical elements of the PS/PDI endstation configured for measurement of the 10× Schwarzschild objective. Light from the beamline is directed upward by a turning mirror at near 45° incidence. The image-plane pin-holes and CCD camera are inclined at 12.1°, normal to the off-axis central ray. A high-speed shutter placed after the K-B mirrors protects the critical optical components from continuous EUV exposure. Black arrows indicate the degrees of freedom of the components. The experimental coordinate system is shown on the left. *Downstream* and *upstream* refer to the directions of photon flux in the beamline, with and against the flux, respectively. *Inboard* and *outboard* are respectively toward and away-from the storage ring.

remains stationary and in focus as the grating angle is adjusted for wavelength selection. To achieve good fringe contrast, the interferometer requires a source coherence-length greater than the largest path-length difference encountered in the interferometer. In a system designed for approximately 50 fringes across the aperture, this requirement translates into a spectral resolution of  $\lambda/\Delta\lambda$  greater than 50. The resolution of the monochromator is therefore sufficient for this experiment, as demonstrated experimentally.

The K-B mirrors are thin carbon-coated silicon substrates that are polished flat and then bent into an approximately elliptical shape. Transverse widths of the mirrors are varied in such a way as to enable them to be bent into the proper final shape when bending forces are applied near the ends (James Underwood, personal communication).

The configuration of the interferometer endstation is shown in Fig. 5. To illuminate the Schwarzschild objective vertically, a flat, multilayer-coated turning mirror, mounted at an angle-of-incidence near 45°, is placed between the K-B and its focus, directing the beam upward. The turning mirror is

held on a kinematic Gimbals mount which pivots about the designed point-of-incidence of the beam with the mirror. The angle and longitudinal position of the mirror mount is manually adjustable using three micrometers that are attached to a self-contained, detachable stage unit. The adjustable beam angle and position facilitate beam alignment and enable the investigation of wavefront aberrations across the field-of-view of the optic. Within the field-of-view, wherever the object pinhole is placed the beam may be brought to the proper angle and position through the object-plane.

With a minor focusing error (since remedied) in one of the components of the monochromator, the bandwidth was approximately  $\lambda/\Delta\lambda \sim 200$ , or 0.067 nm full-width at half-maximum (FWHM) at 13.4-nm wavelength. The near-45° multilayer-coated turning mirror, designed for peak reflection at 13.4 nm, has a measured full-width at half-maximum bandpass of 0.9 nm, considerably wider than that of the monochromator. In principle, the exit slit of the monochromator controls its transmitted bandwidth. Since the vertical mirror in the K-B pair forms an image of the exit slit in the object-plane, if the K-B system were diffraction-limited, then the exit slit would be redundant with the object pinhole — the size of the pinhole would determine the transmitted bandwidth. Before a major overhaul in the summer of 1997, the performance of the K-B system was *aberration-limited*, meaning that the image of the exit slit in the object-plane was substantially blurred. Therefore the object pinhole was not performing as a wavelength filter.

EUV light from the beamline is strongly polarized in the inboard/outboard direction, parallel to the floor. On axis, the first-harmonic light from the undulator is polarized, and the glancing-incidence beamline optics do not significantly affect the direction of the polarization. The near-45° multilayer mirror is also a polarizing element (see Appendix 3). By directing the beam vertically, this mirror selects the inboard/outboard polarization approximately 12 times more efficiently than the vertically polarized components.

### 6.2.3 Hector’s Magic Flange

In the focal plane of the K-B, coincident with the object-plane of the test optic, the sub-micron object pinhole is held in a kinematic mount attached to a three-axis stage, shown in Fig. 6. The stage enables horizontal translation of the object pinhole to position it within the narrow beam, and vertical translation to bring the pinhole into the desired object-plane. This versatile stage and housing arrangement has come to be called “Hector’s Magic Flange” (HMF) after its designer, Hector Medeck. The flange is held between a pair of bellows that enable motion over a range of approximately 1 cm (vertical)  $\times$  5 mm  $\times$  5 mm.

A removable pinhole holder, shown in Fig. 6, consists of a metal cylinder with a tapered conical tip. This tip fits kinematically into a conical well of a slightly larger angle, mounted inside the HMF. Part of the cylinder is machined away and a flat area is created that allows the pinhole to sit on the axis of the cylinder. A hole is bored below the pinhole position to allow the light to reach the pinhole. The rotation angle of the cylindrical pinhole holder is set by a flexible arm attached at 90° to the cylinder axis. This



arm snaps into a grooved holder mounted to the HMF outside of the vacuum chamber. An o-ring seal is formed where the holder enters the HMF — the holder passes through an open cylindrical screw that, when tightened, compresses the o-ring against the holder. Figure 6 also shows a configuration for visible-light interferometry in which the pinhole holder is modified to introduce a polished, tapered-capillary fiber-optic source and a 45° turning mirror to bring a laser source into the object plane.

A small 1.5-mm-diameter circular *orifice* at the bottom of the HMF acts as a differential aperture separating the vacuum of the chamber from the rest of the beamline. Here, a three-position stage gives the HMF additional functionality. In one position, the orifice is open to allow the EUV beam to pass. Second, the orifice may be sealed with a small glass window-valve allowing the co-propagating visible-light beam from the ALS to be used for visible-light system alignment while the interferometer chamber is vented. This feature has proven to be an *invaluable* aid. In its third position, the stage contains a photodiode that can be positioned immediately above the orifice to aid in EUV alignment and diagnostics.

Also connected to the HMF is a thin capillary oxygen inlet line. It is widely known that the presence of a small pressure of oxygen is useful in the abatement of hydrocarbon contamination in EUV optical systems. Here the capillary directs a jet of oxygen gas into the HMF, directed toward the entrance-side of the object pinhole. The capillary conducts oxygen through a needle-valve so that a predictable and constant pressure of oxygen may be used. On a base pressure of  $5 \times 10^{-7}$  torr, the oxygen pressure is typically  $2 \times 10^{-4}$  torr in the interferometer chamber. Some oxygen flows through the orifice into the 45°-mirror chamber and the K-B mirror chamber. Although it has not been carefully characterized *in situ*, the presence of this low oxygen pressure may in fact be beneficial in removing contamination from those optical surfaces.

Aligning the narrow, focused EUV beam through the sub-micron object pinhole is not trivial. When the system is far from alignment and there is no detectable beam flux through the object pinhole, creative

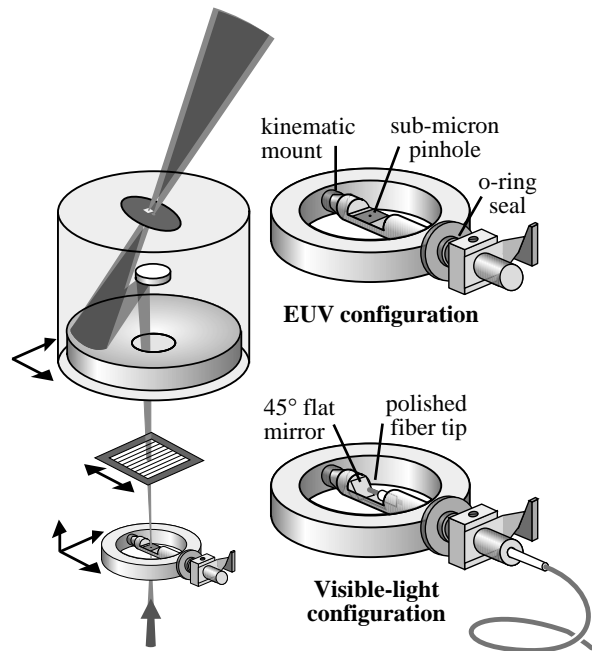


**Figure 6.** Illustration of *Hector's Magic Flange* (HMF), which performs as a object pinhole kinematic mount on a three-axis stage. Visible light may be introduced into the chamber via an optical fiber with a polished tip in conjunction with a small 45° mirror. A 1.5-mm orifice at the bottom of the flange (not shown) acts as a differential aperture for the vacuum system. A three-position stage can bring a detector or a small glass window valve onto the top of the orifice.

measures are required. First, to ensure that the beam enters the 1.5-mm-diameter orifice at the entrance to the HMF, the area surrounding the hole is painted with phosphor. Using a viewport located above the 45° turning mirror and a small, adjustable, strategically-positioned mirror, the orifice may be observed when the system is at vacuum. The beam spot is clearly visible on the phosphor paint when it fails to enter the orifice. The detector on the three-position stage immediately above the orifice can be used to center the narrow beam through the orifice.

Once it is known that the beam clears the edges of the orifice, the object pinhole must be positioned in the beam. Here, to establish the location of the beam within the object-plane a thin mylar membrane is placed in the object-plane using a separate but identical pinhole holder. In a matter of seconds, the focused EUV beam burns through the mylar, leaving a visible burn-spot on the otherwise transparent membrane. In a microscope fitted with a copy of the HMF kinematic mount, the object pinhole can be hand-positioned in a matter of minutes into the proper location based on the mylar burn spot. Achieving the proper position within 10 or 20  $\mu\text{m}$  is usually satisfactory for locating the pinhole *in situ*. A separate strategy involving an accurate stage that duplicates the orientation of the HMF translation axes and kinematic mount could simplify the alignment process by eliminating the need for fine hand-positioning. However, the recent installation of highly sensitive detector electronics has made locating pinholes from scratch easier and much less time-consuming.

#### **6.2.4 Other Stages and Components**

The elements of the beamline that are most difficult to adjust are the bendable and tiltable K-B mirrors. Once a satisfactory configuration of the K-B mirrors was found, and the nominal focal position was acceptable for the illumination of the Schwarzschild objective, no further adjustments of the K-B mirrors were made.

The particular K-B mirror substrates used during the time of these interferometry experiments were known to be of poor quality, yet these were the only mirrors available at the time. The longitudinal distribution of light near the imperfect K-B focus allows the object pinhole to be placed within a range of several hundred microns without suffering a dramatic loss in flux. Near the focal plane, the distribution of light is measurable by scanning the three-dimensional position of the object pinhole while using a retractable photodiode-detector placed several centimeters above the object plane to measure transmission. While the poor performance of the K-B system created a larger than expected focal spot and caused a lower than expected photon flux through the object pinhole, this unintended property of the beamline actually facilitated the positioning of the object pinhole over a broad range (1 cm) of longitudinal positions. K-B mirrors of much higher quality have since been fabricated, installed, and tested.

With the beam and object pinhole held stationary, lateral alignment of the image point is performed

by two-axis horizontal translation of the test optic. This translation with respect to a stationary object point takes advantage of the 10× demagnification to enable positioning of the image point with better than 0.1- $\mu\text{m}$  resolution. The optic itself sits on a bearing-stage, and a pair of Picomotors are used to move the optic through several millimeters of travel. The Picomotor translations are demagnified 2:1 using flexural pivots and are coupled to the motion of the bearing through a pair of wobble-pins. Linear Variable Differential Transformers (LVDTs) are used to monitor the positions of the Picomotors (and hence the bearing on which the optic rests) through the vacuum chamber walls.

A coarse grating beamsplitter is placed between the object pinhole and the entrance aperture of the test optic. The grating, typically 18- $\mu\text{m}$ -pitch, is made of a gold absorber pattern on a 100-nm-thick silicon-nitride membrane, with 5×5-mm<sup>2</sup> area (fabricated by Dino Chiarlo). In order to conduct measurements with the fringe patterns in two orientations, 90° apart, two separate gratings and grating-stages are used. To enable phase-shifting, the two gratings are held on separate one-dimensional horizontal translation stages, each with motion in the direction perpendicular to the rulings. The grating stages are attached to coarse translation mechanisms that allow the gratings to be completely retracted from the beam.

Custom-designed hardware (by Paul Denham) and software (by Joshua Cantrell and the author) are used to control the three axes of the HMF stage (object pinhole positioning), the grating stages, and the two axes of the Schwarzschild objective. The motor-control software programs were created to be very responsive with a high degree of interactivity and the inclusion of many features that facilitate the requirements of the interferometry experiments. Motor positions are adjustable using on-screen control panels containing scalable grid-displays of present and previous positions in three-dimensions, where appropriate. The programs include a position memory feature that allows tens of previous locations to be stored and recalled, rapidly returning the system to a previous state. Automatic *raster* and *spiral* scanning features are included to aid in the location of pinholes and other points of interest. The grating-control program stores calibrated step values to facilitate phase-shifting, and it keeps track of step numbers to aid in data collection.

#### **6.2.5 Pinhole Spatial Filters**

The quality of the pinhole-diffracted waves is the single element that has the most substantial impact on the accuracy and precision of the interferometer. The pinholes are the most critical elements of the interferometer; therefore the use of high quality pinholes in the object- and image-planes is imperative. Because of their small size, and because of their use as diffractive elements, *high quality* for pinholes has a functional definition based on their performance as spatial filters, *in situ*.

The commercially-available laser-drilled object pinholes used are on the order of 0.5- $\mu\text{m}$  diameter, approximately one-fourth of the diameter required to produce a diffraction-limited beam at 0.008 NA. Evaluation of the quality of the diffracted waves is presented in Sections 6.3 and 8.3.

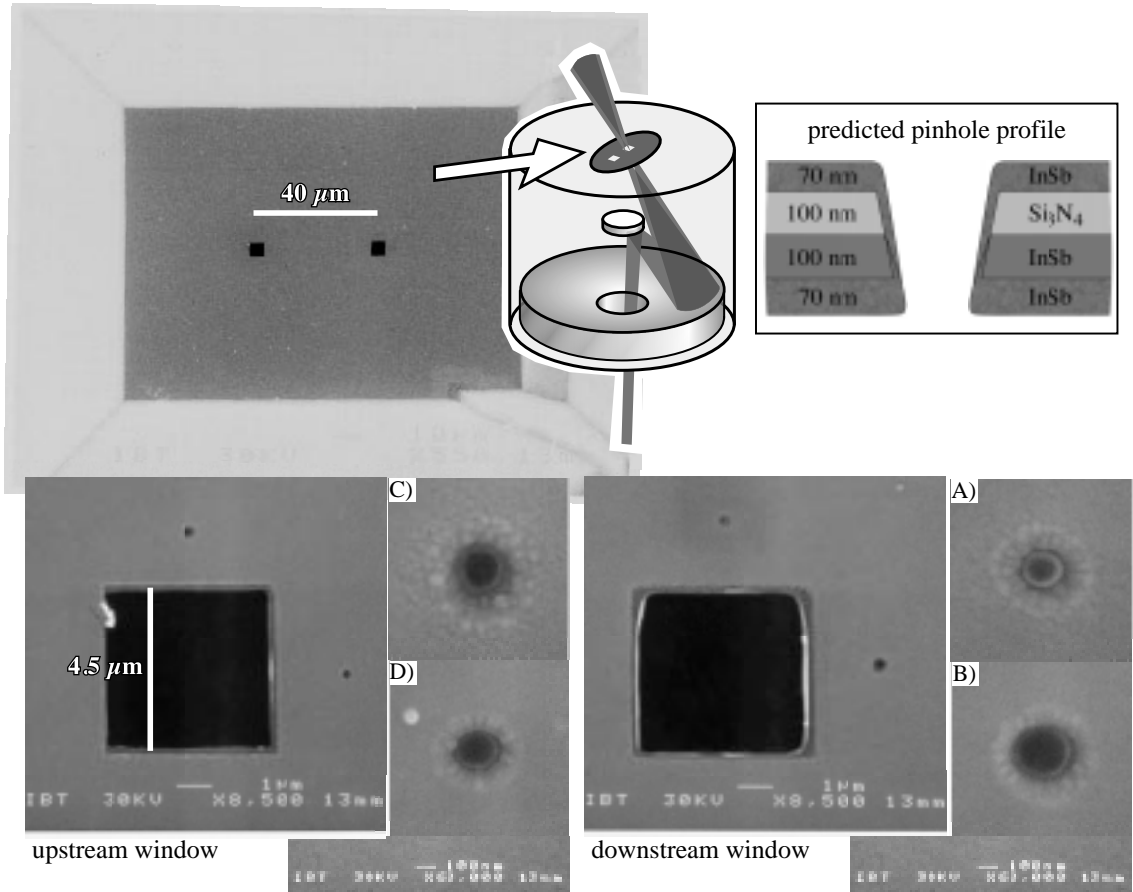


**Figure 7.** The image-plane reference pinholes used in the PS/PDI experiments were fabricated by focused ion-beam lithography in a 100-nm-thick  $\text{Si}_3\text{N}_4$  membrane with a 70 nm InSb absorber layer. After the *open-stencil* pinholes and window were etched completely through the membranes, additional InSb absorber layers were deposited on the two sides of the membrane. The membrane contains two window and pinhole patterns separated by 40  $\mu\text{m}$ , defining two closely-spaced field points displaced in the upstream-downstream direction. The pinholes were fabricated at Intel. Pinhole size is discussed in Section 6.4.

Two sets of image-plane pinhole membranes were used in the PS/PDI experiments described here. The first set of pinholes was made of a patterned gold absorber layer on a solid silicon-nitride membrane, fabricated by electron beam lithography. The pinhole pairs consisted of two sub-100-nm reference pinholes adjacent to a square window, 5.0  $\mu\text{m}$  on edge, with center-to-center separations of 4.5  $\mu\text{m}$ . This first pinhole membrane was abandoned because of problems created by contamination on the solid membrane. Without the benefits of oxygen gas, the membranes became unusable in a matter of minutes, as damage to the window membrane obstructed the transmission of the test beam.

A second set of image-plane pinholes, shown in Fig. 7, was fabricated on a membrane consisting of a 100-nm-thick silicon-nitride ( $\text{Si}_3\text{N}_4$ ) support membrane, with a 70-nm-thick indium-antimonide (InSb) absorber layer. An open-stencil pattern of pinholes and windows was created using focused-ion-beam lithography to *drill* open holes in the membrane. Following the pattern definition, additional 70-nm-thick lay-

ers of InSb were deposited on both sides of the membrane to increase absorption and reduce the pinhole size. The  $1/e$  intensity transmission depths of InSb and  $\text{Si}_3\text{N}_4$  for 13.4 nm wavelength light are 15.2 nm and 117 nm respectively; therefore, based on thicknesses of 100 nm  $\text{Si}_3\text{N}_4$  and 240 nm InSb, the transmissivity of the membrane is expected to be on the order of  $5.9 \times 10^{-8}$ . Unlike the semi-transparent PDI pinhole membrane, the PS/PDI membrane is required to be opaque.

This second pinhole membrane was used for all of the PS/PDI measurements reported here. These four pinholes were used in literally thousands of interferogram exposures over the course of two months. For reference, these four pinholes have been here labeled, A, B, C, and D, as indicated in Fig.7. The diffraction characteristics of these pinholes are discussed in Section 6.4.

In this configuration of the PS/PDI for Schwarzschild objective measurement, the image-plane pinholes are manually pre-aligned and remain stationary with respect to the moving test optic. For repeatable pinhole positioning, the pinholes are attached to a kinematic mount that rests on the three balls that define the image-plane. The mount holds the pinholes inclined at  $12.1^\circ$ , normal to the central ray of the off-axis beam. The tops of the balls fit snugly into three shallow, radial “V” grooves on the under-side of the mount, creating three distinct and repeatable positions of the mask, approximately  $120^\circ$  apart. This three-way positioning facilitates measurement of all three sub-apertures of the Schwarzschild objective without modification of the pinhole mounting.

The pattern of the pinhole membranes can be arranged in many ways. Using an array of pinhole/window patterns facilitates wavefront measurement across the field-of-view of the test optic without repositioning the image-plane pinholes. Here, one difficulty is the requisite  $12.1^\circ$  inclination of the pinhole membrane that causes pinholes in an array to occupy different longitudinal planes. At this time, research has been proposed to investigate the importance of keeping the pinholes at normal incidence to the central ray. Until this evaluation has been completed, the inclination of the pinhole plane should be maintained. The first effect of the membrane tilt is that field points separated by 40  $\mu\text{m}$  laterally (a typical distance) differ in longitudinal position by 8.4  $\mu\text{m}$ . With a  $10\times$  demagnification optical system, each micron of longitudinal image-plane position change requires a 100  $\mu\text{m}$  adjustment of the object-plane position: a 8.4- $\mu\text{m}$  image-plane change requires a (large) adjustment of 840  $\mu\text{m}$  from the object-plane.

#### **6.2.6 High-Vacuum-Compatible High-Speed Shutters**

A reliable, high-vacuum-compatible beam-shutter is of prime importance for the EUV interferometer. The shutter, placed beyond the K-B mirrors in a position where the beam size is approximately 4-mm-diameter, protects the critical and sensitive interferometer components from constant, intense EUV exposure. The shutter must be synchronized with the CCD control hardware to prevent exposure during read-out. Two novel shutters have been custom designed and implemented in the interferometry experiments.

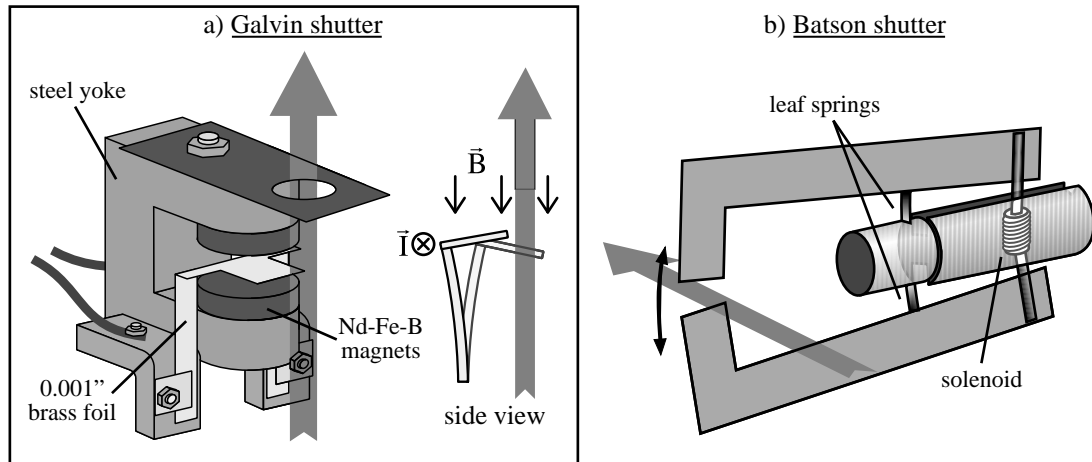


**Figure 8.** High-vacuum-compatible high speed shutters are required to protect the optical components from constant exposure, and to ensure the proper operation of the CCD detector. Two shutters have been developed for this purpose. a) A shutter designed by James Galvin operates based on the Faraday effect. b) To achieve greater travel and faster operation, a second shutter designed by Philip Batson was installed after the interferometric measurements described in this thesis had been performed.

These are shown in Fig. 8.

A compact shutter designed by James Galvin, shown in Fig. 8(a), operates based on the Faraday effect: a current-carrying shutter flap moves within the strong stationary field created by a pair of strong Nd-Fe-B magnets held in a steel yoke. This particular shutter functioned successfully through months of daily operation, but suffered from a short range of motion (below 4 mm) that caused it to block a portion of the available beam.

In the active area, the measured magnetic field is approximately 0.5 Tesla. The flexible shutter flap is created from a single piece of 1-mil brass foil machined or hand-cut and folded into the proper shape. The shutter has a travel of approximately 3 mm, carries approximately 1-amp peak current, and operates with a minimum useful open time of approximately 50 msec. One or both of the clamps that hold the shutter flap must be electrically isolated from the vacuum chamber.

During the development of the shutter, several conductive non-magnetic materials were evaluated for use as the shutter flap. One-mil-thick (25.4  $\mu\text{m}$ ) brass met the criteria for high flexibility, light weight, vacuum compatibility, and shape-retention. One important design flaw was discovered and addressed early on. When the foil was folded sharply near the position where it is required to bend, the joints were observed to fail after only a few hours of operation. This problem was overcome with the design shown in Fig. 8(a), wherein the *legs* of the flap are neither bent sharply nor creased in any way. Bending occurs in a gradual arc along the relatively long length of the foil. There is no stress applied to the fold which causes the flap to project forward at 90°.

One element not shown in Fig. 8(a) is a motion restrictor that limits the backward (into the yoke)

travel of the flap. With the large applied forces and the narrow but deep magnetic gap, this restrictor is required to prevent the shutter flap from sticking to the magnet surfaces. The restrictor consists of a thin glass tube on the end of a wire bent into a “C” shape and epoxied into position.

To achieve greater travel and faster operation, a new shutter designed by Philip Batson was used. The shutter arms open rapidly, pulled by the force of a pair of small magnets inside a solenoid symmetrically placed between the arms. The arms are pulled against the force of a bent leaf-spring that holds the arms closed in the absence of current. The minimum useful exposure time enabled by the shutter is approximately 0.05 seconds.

Once again the arms of the shutter are electrically isolated from the vacuum chamber. In this second implementation a current meter attached between the shutter arms and ground enables the shutter to function as a photocurrent detector. When the EUV beam falls on the closed leaves of the shutter, the current from the shutter is typically on the order of 1  $\mu\text{A}$ .

### **6.2.7 Beam Detectors**

Identical to the EUV PDI experiments (Chapter 3), data is recorded with a back-thinned, back-illuminated, un-coated,  $1024 \times 1024$  pixel, 1-square-inch area, 16-bit Tektronix CCD camera optimized for EUV detection. The CCD is mounted at an angle of  $12.1^\circ$  from the vertical to receive the central ray of the test beam at normal incidence. The detector is placed approximately 12 cm beyond the image plane.

Two Hamamatsu GaAsP photodiode detectors are used to monitor the beam flux. The detectors have  $5 \times 5\text{-mm}^2$  area. As mentioned in Section 6.2.3, one detector is held just above the HMF orifice. This detector is primarily used to center the beam within the 1.5-mm-diameter orifice. A second detector is held on a retractable arm in a plane just above the grating stages. This detector measures the beam current *after* the object pinhole and is used to optimize the position of the object pinhole.

## **6.3 THE TEST WAVE**

The simple illumination pattern of the test optic reveals a great deal of information about the quality of the Schwarzschild objective and its multilayer coatings. With no image-plane windows or pinholes, the optic is illuminated at 13.4-nm wavelength using a  $\sim 0.5\text{-}\mu\text{m}$ -diameter object pinhole spatial filter. The illumination is recorded with the CCD detector, placed approximately 12 cm beyond the image-plane.

One important characteristic of the Schwarzschild objective is that the concave secondary mirror forms a real image of the primary mirror (the entrance pupil) 7.9 cm beyond the image plane. The image is inverted and is magnified by approximately  $3\times$ . Any visible feature of the primary mirror is projected sharply into this plane. Although the CCD camera is placed several centimeters beyond this plane, large

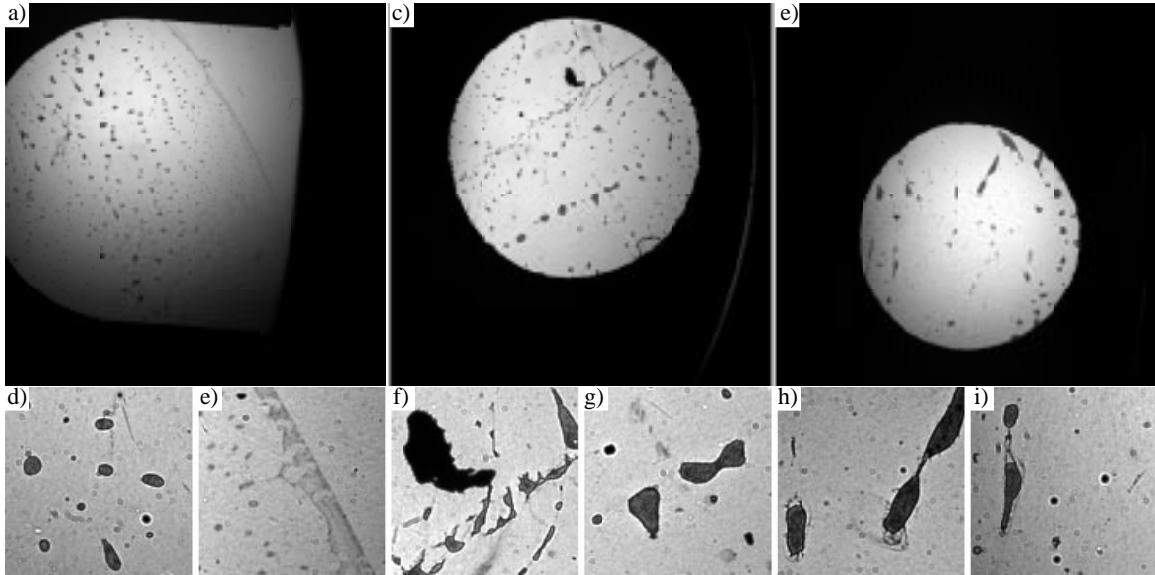


**Figure 9.** Illumination of the 10× Schwarzschild objective reveals a pattern of defects, or *blemishes*, observable as intensity variations in the test beam. Transmission through the three sub-apertures is shown here as recorded by the CCD camera in 1024×1024-pixel images. (a), (b), and (c) are raw data shown in linear scale. (c) The aperture stop does not fully extend to the edge of the mirror surface, allowing a curved sliver of light to pass. Details of several of the blemish regions are shown in (d) through (i), with (d) and (e) taken from (a), (f) and (g) from (b), and (h) and (i) from (c). Each detail is 120 × 120 pixels, subtending an approximate solid angle of 0.024 rad, or 1.4°, representing an area 510-μm-wide on the primary mirror surface. Bright, thin diffraction *halos* are visible along the sharp boundaries of the blemishes because the CCD is several centimeters beyond the plane in which the concave secondary mirror re-images the primary.

defects on the mirrors appear very distinctly, as is apparent in Fig. 9. The ability to observe these features clearly in the pupil is due to the short wavelength used, the narrow cone of rays, and the relatively large size of the blemishes. The features *are* out of focus in the plane of the CCD, and under careful inspection, a small bright ring is observable around every sharp feature.

### 6.3.1 Blemishes

The presence of numerous blemishes in the test optic could be due to defects in the substrate, contamination of the substrate prior to coating deposition, contamination during deposition, contamination of the coating surface, or a combination of these effects. By eye, several dust particles are visible on the mirror surfaces, but the appearance of these streaks and spots suggests that there may be residue left by a wet cleaning process. One attempt at cleaning using de-ionized nitrogen gas was made, but this yielded little observable difference.

With the grating beamsplitter removed, the isolated test beam passes through the image-plane window. In this configuration, an image of the spatially-filtered test beam is recorded with each interferometric measurement. Test beam images from all three sub-apertures are shown in Fig. 10.

### 6.3.2 Illuminating Beam: In Situ Pinhole Size Assessment

The spatially-filtered illuminating beam is the first spherical reference wavefront of the interferom-



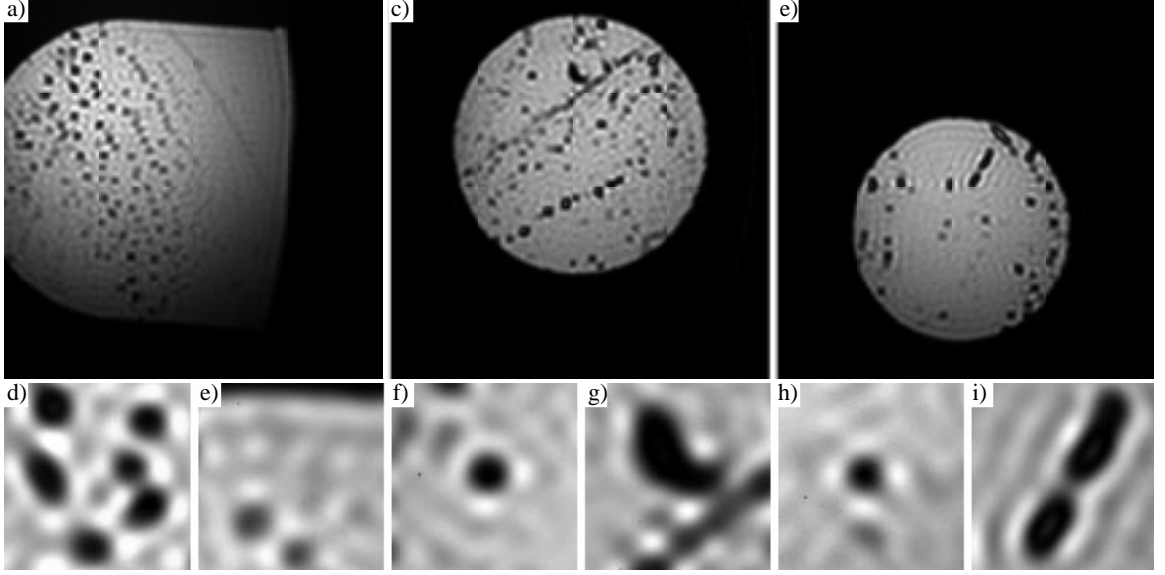


**Figure 10.** Filtered *test beam* images from all three sub-apertures are recorded in the same manner as those shown in Fig. 9. However, with the PS/PDI image-plane pinholes and windows installed, the test beam is spatially filtered by the  $4.5\ \mu\text{m}$  window. As before, the details, (d) through (i) (are  $120 \times 120$  pixels, subtending an approximate solid angle of  $0.024\ \text{rad}$ , or  $1.4^\circ$ ). (d) and (e) are taken from (a), (f) and (g) from (b), and (h) and (i) from (c), although they do not correspond to the same detail regions shown in Fig. 9. The square shape of the spatial filter window is evident in the *rectangular* pattern of ripples that surrounds each defect. This is especially apparent with the smallest “sub-resolution” defects. See Section 5.10 for a discussion of spatial filtering.

eter. Based on observations of the test beam and of the angular rate of intensity fall-off, the size of the object pinhole can be determined approximately. The *actual* size can be determined by other means, such as electron microscopy. However, since the most important property of the pinhole is the quality of the wave diffracted from it, an *effective size* of the pinhole can be defined as the size of the equivalent ideal pinhole that diffracts an Airy-like wave.

By design, the first diffraction minimum of the illuminating beam falls well beyond the NA defined by the entrance pupil. An estimate of the pinhole diameter may be based on the intensity full-width at half-maximum, the known object-side NA angle within the pupil, and an assumption of an Airy-like diffraction pattern. As discussed in Sections 2.3.1 and 4.6.1, the angular distribution of the Airy pattern intensity is

$$I(\alpha / \lambda) \propto \left( \frac{\lambda d}{2\alpha} \right)^2 J_1^2 \left( \frac{\pi \alpha d}{\lambda} \right). \quad (1)$$

$\alpha$  is the direction cosine with respect to the central ray. When the half-angle of the intensity half-maximum  $\theta_{1/2}$  is known, then the pinhole diameter may be calculated empirically from

$$d = \frac{0.514 \lambda}{\sin \theta_{1/2}}, \quad (2)$$

based on Eq. (1). Using the average of two similar measurements of the intensity profile, taken from the

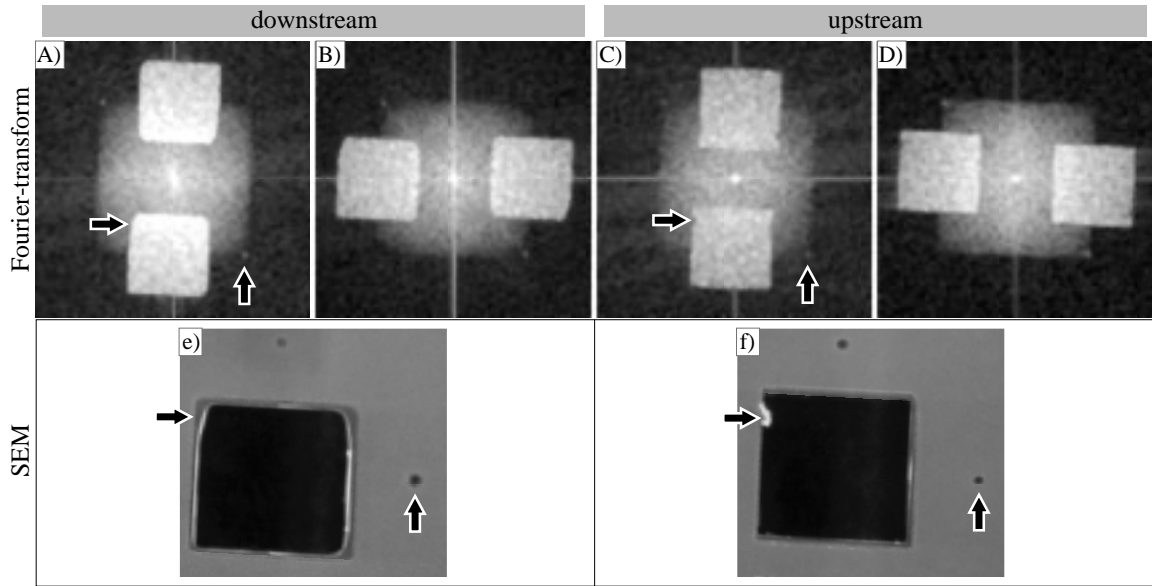


**Figure 11.** (A) through (D) The patterns of the pinholes and the window are clearly visible in the logarithmically-scaled Fourier-transform of the reference pinhole diffraction patterns. Because the (strictly-real) intensity of the diffraction pattern is measured, the Fourier-transform shows polar symmetry. With a single beam centered on one of the reference pinholes, the leakage of light through the window and the second pinhole illustrates the role of the window as a bandpass filter for the reference beam, allowing a range of mid-to-high spatial-frequencies to pass. Reference pinholes (A) through (D) are featured in (A) through (D) respectively. SEM images of the same pinholes are shown for comparison. Irregularities in the shapes of the windows are clearly visible in the Fourier-domain.

test wave measurements, the effective pinhole diameter is estimated to be  $0.76\ \mu\text{m}$ . More than one pinhole was used in the interferometric experiments: after one pinhole had been used to gather the bulk of the interferometric data, several other pinholes were tested. These experiments are discussed in Chapter 8. Experiments to determine the quality of the spatial filtering properties of the entrance pinhole are discussed in Section 8.3.

#### 6.4 THE REFERENCE WAVE

As with the PDI, the quality of the reference wavefront is the most important element for determining the accuracy and precision of the PS/PDI. The size of the reference pinholes largely determines the quality of the spatial filtering they generate. In this section, two ways of determining the effective size of

**Table 1.** Size determination by SEM and at-wavelength diffraction measurements of the four reference pinholes used in the interferometry experiments.

pinhole	SEM			Diffraction		
	$x$ -width	$y$ -width	$d = \sqrt{xy}$	$x$ -width	$y$ -width	diameter
A	137	124	130	168	141	154
B	220	201	210	168	154	161
C	164	171	167	177	173	177
D	163	144	153	172	159	167

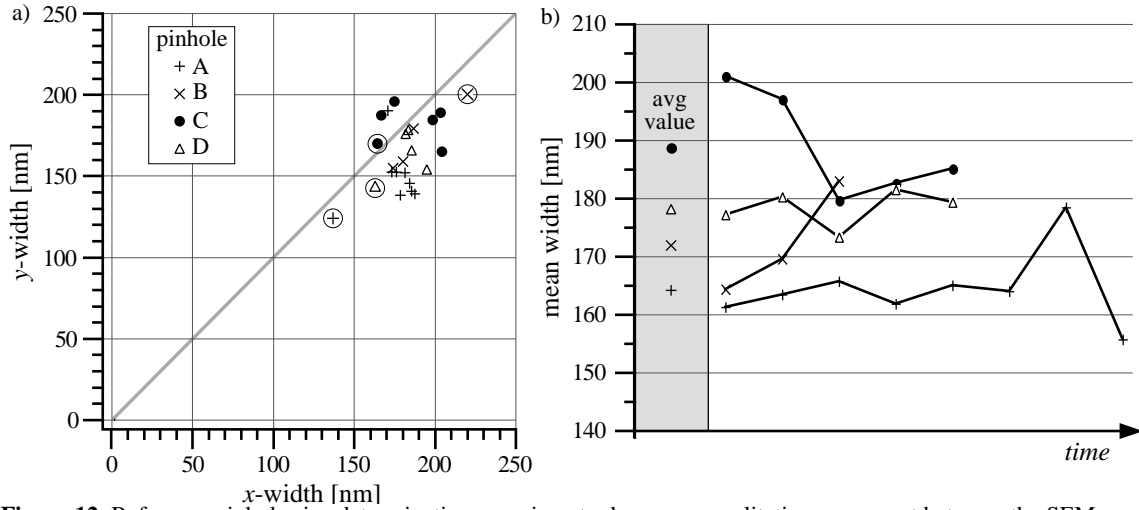


**Figure 12.** Reference pinhole size determination experiments show poor qualitative agreement between the SEM observations, and the measured pinhole diffraction patterns. The averaged data is shown in Table 1. (a) Separate  $x$ - and  $y$ -widths are determined from both the SEM images and the diffraction patterns. Each diffraction measurement is shown in the left graph. The SEM measurements of the same four pinholes are indicated by circled symbols. Over a two month period, diffraction measurements were made occasionally. (b) The time axis indicates only the order in which the diffraction patterns were recorded. The same plotting symbols are used in both graphs.

the reference pinholes are described, and characteristics of the reference waves are discussed. As described in Section 6.2.5, there are four pinholes from one single pinhole membrane under investigation. These pinholes represent two orthogonal directions from two field points. As shown in Fig. 7, the field points are located in the upstream and downstream directions, separated by only  $40\ \mu\text{m}$ .

#### 6.4.1 The PS/PDI Reference Wave

The reference wave in the PS/PDI is considerably different from that of the PDI because of the way in which it is generated. In the PS/PDI, where a beamsplitter produces multiple focused beams in the image-plane, the beam selected as the test beam passes through a (relatively) large window, while an adjacent beam is brought to focus on the sub-resolution reference pinhole. Regardless of the beam separation and the quality of the optical system under test, there will be some overlap. Typically, the most significant consequence of this is the overlap, or *leakage*, of the reference beam through the large window. Since the window sits in the image-plane and is displaced from the center of the reference beam, it behaves as a bandpass filter allowing a range of mid- to high-spatial-frequencies to be transmitted.

In order to characterize the reference pinholes, experiments were done to investigate their diffraction properties. In these experiments, the grating beamsplitter is removed and a single beam is brought to focus on a pinhole under study. These experiments parallel those reported for the PDI pinholes, Chapter 3.

The measured far-field diffraction patterns may be understood from examination of their Fourier-transforms, shown in Fig. 11. Because only the (strictly-real) intensity of the far-field diffraction pattern is measured, the Fourier-transform is Hermitian — its complex amplitude shows polar symmetry. At the

center of the Fourier-transform pattern is a narrow peak representing the spatial frequency content of the highly filtered beam that passes through the reference pinhole. Figure 11, which is logarithmically scaled and smoothed for display, clearly shows the function of the window as a bandpass filter. For comparison, the SEM image of the pinhole window is shown adjacent to the Fourier-transforms. The shapes of the windows, including irregularities, are clearly reproduced in the Fourier-domain. Even the second, unused pinholes are visible in the Fourier-transform as a faint bright peak.

#### 6.4.2 In Situ Pinhole Size Assessment

The sizes of the reference pinholes can be determined in several ways, including SEM and *in situ* diffraction measurements performed *at-wavelength*. While SEM measurements are the most straightforward indicators of size, the widths of the diffraction patterns yield the useful *effective diameters* that would be expected by the assumption of ideal, Airy-like diffraction.

The SEM images of the pinholes (recorded by Larry Murray), taken in reflection mode, are shown in Fig. 11. The maximum widths in the  $x$ - and  $y$ -directions may be ascertained from the apparent open area of the pinholes. The  $x$ - and  $y$ -direction widths are shown in Table 1, along with the geometric mean. These two directions are arbitrary, yet provide some qualitative indication of apparent pinhole ellipticity.

The pinhole diameters are also calculable from the diffracted intensity profile in the same manner used for the estimation of the object pinhole diameter in Section 6.3.2. From Eq. (2), the half-angle at half-intensity is used. To calculate this angle, a small sampling of reference pinhole diffraction patterns is made. The angle-to-pixel ratio for the CCD camera is known from the interferometry experiments to be approximately 0.2 mrad per pixel. To calculate the half-angle, the pinhole diffraction patterns are spatially filtered to remove the mid- and high-frequency content. For each image, a contour is generated automatically, tracing the half-maximum of the intensity in approximately 500 points. From these points, the first moments of the distribution are used to determine the *central* points in the  $x$ - and  $y$ -directions. These are shown in Fig. 12. The mean distance (in pixels) from each contour point to the center is used to calculate the half-angle. Also of interest are the maximum angular widths in the  $x$ - and  $y$ -directions, given in Table 1. As with SEM analysis, these directions are arbitrarily chosen, yet provide a qualitative indication of any ellipticity in the pinholes.

It is clear from the comparison of these two size-determination methods that the SEM images do *not* provide a good indication of the effective pinhole diameters observed in the diffraction measurements. In fact, the pinhole that appears largest in the SEM images, pinhole B, produces a diffracted wave that is the second-smallest of the four.

## 6.5 FOURIER-TRANSFORM ALIGNMENT METHOD

Once the illuminating beam is aligned and the object pinhole position is optimized for peak flux, the most difficult procedure is bringing the reference beam onto the tiny reference pinhole, on the order of 100-nm diameter. Alignment proceeds by lateral translation of the test optic, taking advantage of the 10 $\times$  demagnification to achieve fine adjustment of the lateral beam position in the image-plane. When the system is aligned, or nearly aligned, interference fringes become visible and the alignment proceeds by optimizing the appearance of the fringes, looking for uniformity and complete coverage of the illuminated area. When the system is misaligned, even slightly, the fringe pattern is not visible and there are few clues available to bring the system toward proper alignment.

One somewhat effective method is to observe the *square-ish* ring pattern that surrounds the small blemishes. When the system is properly aligned and the test beam passes through the center of the window, the rings are symmetric top-to-bottom and right-to-left. Using this indicator is equivalent to understanding the Fourier-domain filtering performed by the window.

A much more effective technique uses the Fourier-domain *directly*. Since the recorded intensity is the far-field diffraction pattern of the image-plane field, a simple Fourier-transform provides a mathematical *image* of the field in that plane. For each image recorded, the fast Fourier-transform (FFT) algorithm can be implemented rapidly and the results displayed with logarithmic scale, giving immediate visual feedback on the position of the beam within the window or pinhole. Such a system, developed by the author

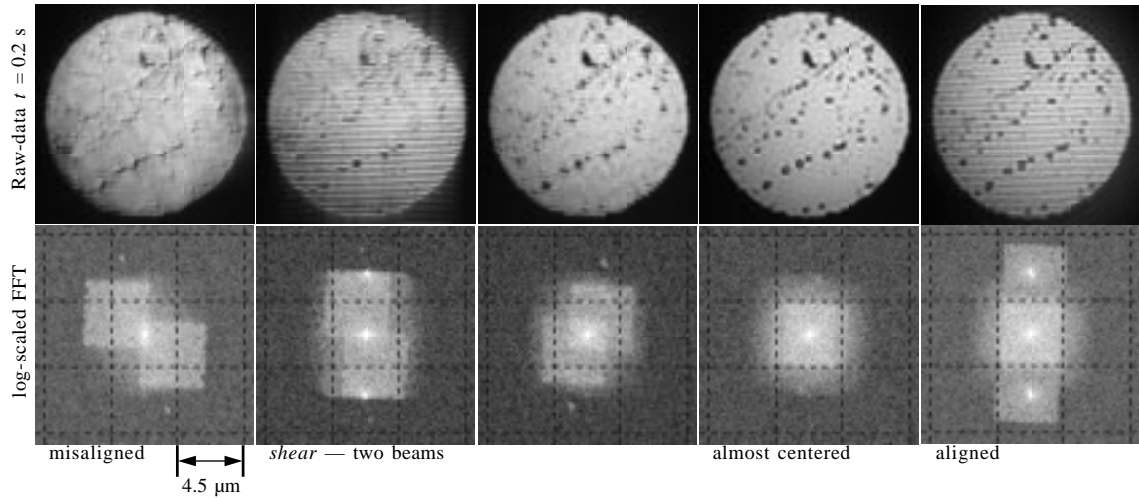


**Figure 13.** The Fourier-transform alignment method facilitates the otherwise-difficult alignment of the reference beam through the tiny reference pinhole in the image-plane. The raw intensity data collected by the CCD detector (top row), with 0.2 second exposure time and  $4 \times 4$  pixel hardware binning, is the far-field diffraction pattern of the field in the image-plane. As such, the Fourier-transform (bottom row) reveals the distribution of light in the image-plane. Since the real-valued intensity is measured, the Fourier-transform is Hermitian, accounting for the redundant image.

This typical series of images was recorded during system alignment. As the lateral position of the test optic is adjusted, the beam becomes more centered in the window until the PS/PDI fringe pattern is clearly visible. The image marked as “shear” indicates that two beams are passing through the window, similar to a lateral shearing interferometer. However, in this geometry both beams clip the edges of the window and are thus of poor quality.

and successfully implemented as of October 1997, has greatly enhanced the alignment procedure. Images are recorded with sub-1-second exposure times, and the FFT is displayed almost immediately, adjacent to the raw intensity data. As the fringes become visible, the first-order peaks appear above the background.

Since the CCD measures only the (strictly-real) far-field intensity pattern and the phase information is unavailable during the alignment process, the Fourier-spectrum is Hermitian — the complex amplitude of the FFT shows a redundant polar symmetry. Several typical interferogram and Fourier-transform images are shown in Fig. 13.



# *Wavefront Measurements and Imaging*

---

<b>7.1 INTRODUCTION</b>	<b>128</b>
<b>7.2 WAVEFRONT MEASUREMENTS</b>	<b>128</b>
7.2.1 Determination of the Raw Phasemap	
7.2.2 Establishing a Coordinate System — Sub-Region Definition	
7.2.3 Wavefront Surface Fitting	
7.2.4 Sub-Aperture A	
7.2.5 Sub-Aperture B	
7.2.6 Sub-Aperture C	
7.2.7 Error Analysis	
7.2.8 Zonal Fabrication Error	
<b>7.3 IMAGING EXPERIMENTS</b>	<b>138</b>
7.3.1 Experimental Results and Predicted Behavior	



## 7.1 INTRODUCTION

The central goal of this thesis research is the development and demonstration of at-wavelength EUV interferometry capable of accurately measuring lithographic-quality optical systems. The importance of this capability lies in its the ability to predict imaging performance. In this chapter, wavefront measurements from all three sub-apertures of the 10× Schwarzschild objective are presented. These measurements reveal the nearly diffraction-limited quality of this optical system at the same time as they explore the performance of the interferometer. Subsequent to the interferometric characterization, this optic was used in a series of high-resolution imaging experiments at Sandia National Laboratory.; the results of those experiments are also presented here. As will be discussed, these results show strong agreement with imaging simulations based on the measured wavefront.

## 7.2 WAVEFRONT MEASUREMENTS

This section contains the wavefront measurements of all three sub-apertures of the 10× Schwarzschild objective. Investigations were conducted in the same way for each sub-aperture, with the Schwarzschild objective simply rotated by 120° about its optical axis to bring the proper sub-aperture into position. Relative to sub-apertures B and C, a large number of data sets were recorded of sub-aperture A at 13.4-nm wavelength. For this reason, estimates of the interferometer’s precision are all based on measurements of sub-aperture A.

To measure the system wavefront at a given field point, two phase-shifting measurements are performed using orthogonal fringe directions (i.e. beam separation directions). This is necessary to remove a geometric coma systematic error related to the beam separation (Section 5.5). A pair of orthogonally-aligned grating beamsplitters is used sequentially, to create the two directions of the fringe patterns. The test beam is chosen to be the zeroth-order beam from the grating; it passes through a stationary point in the image-plane window. The reference beam is one of the first-diffracted-order beams from the grating. In each orientation, the reference beam is brought to focus on a reference pinhole that is one of two pinholes placed at 90° with respect to the image-plane window (see Sections 5.11 and 7.2.5 for the design). These two wavefront measurements are combined to remove the geometric coma systematic error using the method described in Section 5.5.2.

From analysis of the four reference pinholes used (two field points were tested), one fact has become clear: because of its large size, pinhole C does not produce a reliable reference wavefront. The wavefront variation observed from this one pinhole renders measurements performed with it unusable. Since individual field-point measurements require the use of *both* pinholes in a pair, data from the *upstream* field point, which use pinhole C, are not presented. In addition, because of the noticeable deteri-

oration in system performance and fringe contrast of the sub-aperture A interferograms that occurred after re-alignment of the system, wavefront data taken after the re-alignment are not included. (This is the “April” data discussed in Section 8.6. The loss of fringe contrast is demonstrated in Section 8.11.)

### 7.2.1 Determination of the Raw Phasemap

Beginning with the raw interferometric data recorded with the CCD camera, the individual exposures are normalized to compensate for the steadily decreasing electron-beam current of the Advanced Light Source. During a measurement series of five interferogram exposures, the current typically decreases by less than 0.5%. Using the least-squares method of phase-shifting analysis (Section 12.2.3) with the Fourier-Transform Method of Phase-Shift Determination (Section 12.4.2), the phase is calculated at every point in the domain. The least-squares technique uses the temporal-domain data to independently calculate the phase at each point. Therefore, it is not necessary to limit the calculations to the sub-region of interest. The modulo  $2\pi$  phasemaps are unwrapped using the robust Fourier-Transform Guided Unwrapping method (Section 13.5) to overcome the high density of *bad* data points associated with the numerous localized blemishes.

The raw unwrapped phase data is shown in Fig. 2 (in the following section, where the sub-region definition is discussed). From the line-out taken in the middle of the sub-region, a high level of noise is apparent. This characteristic of the raw phase data demonstrates why the simple unwrapping techniques fail. The Fourier-Transform Guided Unwrap method was developed specifically to address this difficulty.

### 7.2.2 Establishing a Coordinate System — Sub-Region Definition

In order to successfully compare or combine measurements performed at different times, it is *essential* to establish a consistent coordinate system fixed to measurable positions in the test optic. Even small displacements or rotations between measurements can yield false wavefront differences. The magnitude of these differences is simply related to the wavefront slope (or *derivative*) at any point of comparison.

Virtually any set of clearly observable fiducial markings in the pupil can in principle serve as a reference for the establishment of a consistent coordinate system. For the measurements of the Schwarzschild objective, the distinctive pattern of blemishes in each aperture *became* the fiducial. Using the isolated test beam images (Section 6.3) recorded concurrently with each phase-shifting data set, a single, universal coordinate system was established for each sub-aperture. First, one test beam image was declared to be the *reference*. Then, using the positions of the blemishes as a guide, test beam images from each data set were aligned until the optimal image translations were ascertained. This optimization was performed *manually* by the author using image subtraction techniques. In the future, this painstaking process could be automated by the introduction of an well-designed fiducial system and by the implementation of a relatively simple software algorithm to compare pairs of test beam images.

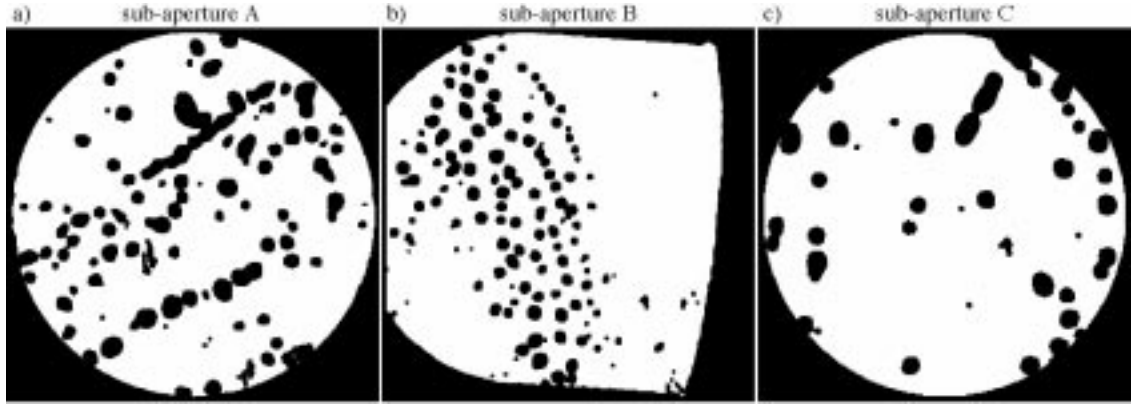


**Figure 1.** Sub-regions used for data analysis in sub-apertures A, B, and C. The blemish regions are removed automatically based on the mid- to high-spatial frequency intensity variations of the measured test beam. The three sub-regions are 659, 830, and 564 points wide and they contain 279188, 503569, and 224470 valid data points, respectively.

Once the relative positions of the various data sets have been brought into agreement, the next step is the establishment of the sub-region containing the valid data for analysis. Interferometrically there are many ways to determine which data points are valid. Some methods are based on fringe contrast or measurement uncertainty (Robinson 1993): these typically apply a threshold function to establish a minimum contrast allowed for inclusion. In this case, such methods are problematic and ineffective for two reasons: first, edge-effects near the blemishes cause unpredictable results and may unintentionally include bad data points in the sub-region. Second, and more importantly, low fringe contrast alone is not a clear indicator of invalid data. A second class of data validation techniques uses information obtained from the phase unwrapping to determine which points are to be excluded (Huntley 1989, Kreis and Juptner 1989, Robinson 1993, Charette and Hunter 1996). Given the high computational demand of this technique, and the desire for a more straightforward approach based on the exclusion of the blemishes, a different method is required.

Because the fringe coverage is very good across the entire aperture for all of these measurements, the sub-region determination method chosen for this application uses the intensity of the test beam as an indication of data validity. The test beam image is compared to a low-pass-filtered version of itself, and a threshold is applied to the ratio. In this way, the localized blemishes are quickly removed and the abrupt edges of the domain are easily found. Following the determination of valid data points, a circular region reaching almost to the edge of the domain is selected. This region becomes the *unit circle* in the normalized detector coordinate system (Section 5.2.2). Since the sub-apertures are slightly elliptical (Section 6.2.1) and irregular in shape, some points at the edges are trimmed. Figure 1 shows the sub-regions defined for each sub-aperture according to this method. Points included in the analysis are shown in white. The numbers of individual points used in wavefront fitting on sub-apertures A, B, and C are 279188, 503569, and 224470,

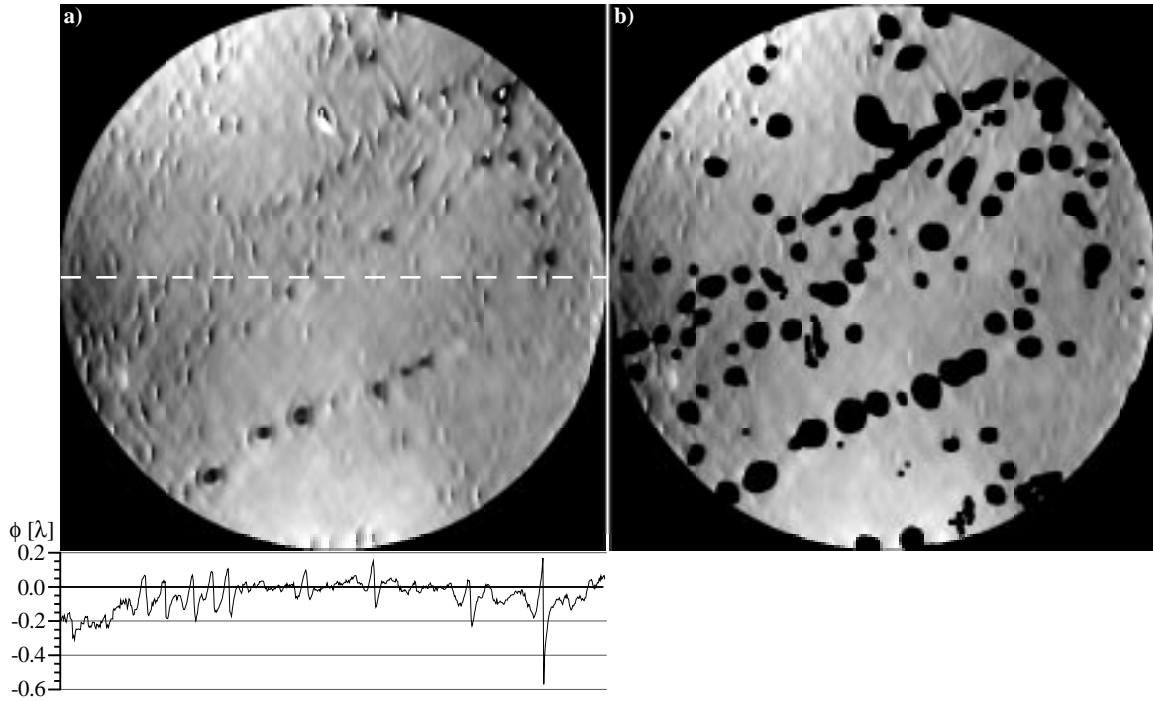


**Figure 2.** (a) Raw phasemap data from one single phase-shifting series representing sub-aperture A. Only the 659-pixel-wide circular sub-region of data is shown. The line-out below (a) is taken from the middle of the sub-region and shows the magnitude and density of the high-frequency phase components that severely complicate the unwrapping and analysis. The sub-region chosen for analysis eliminates most of the problematic regions, without affecting the measurement of the underlying low-spatial-frequency aberrations. (b) Only the points *included* in the wavefront analysis of this sub-aperture are shown.

respectively. Compare the pattern of these sub-region maps to the test beams shown in Section 6.3.

Once the sub-region is determined, wavefront analysis may be performed. To facilitate understanding of the aberrations present in the system and to reduce the effects of mid- to high-spatial-frequency components, surface fitting to the Zernike polynomials is performed. Figure 2(a) shows a raw unwrapped phasemap from a single phase-shifting series of sub-aperture A; here only the points within the full circular sub-region chosen for analysis are shown. Below Fig. 2(a), the line-out shows the severity of the high-frequency noise present in the raw data. The sub-region chosen for analysis excludes the most problematic points from the raw phasemap. When the troublesome points are excluded, the phasemap appears as in Fig. 2(b).

It is very important to remove bad data points from the sub-regions used for wavefront surface fitting. Wavefront fitting is noticeably affected when these points with their spurious phase values are not removed. The irregular patterns and large numbers of points excluded from the circular sub-regions require that special attention be paid to the polynomials used for the analysis. The Zernike polynomials are *not* orthogonal over these irregular domains, and the simplest methods of polynomial fitting will produce unpredictable results.

### 7.2.3 Wavefront Surface Fitting

Chapter 15 addresses wavefront surface fitting in general, and Section 15.5 describes the Gram-Schmidt process of wavefront surface fitting that is used to fit the conventional set of Zernike polynomials on these irregular domains. Based on the Zernike polynomials, an intermediate set of polynomials is generated that is orthogonal over the measurement domain. Once this set is known and the transformation matrix between the two sets has been determined, analysis may be performed with a minimum of uncertainty. The first 37 Zernike polynomial coefficients which describe the low-frequency *figure* aberrations

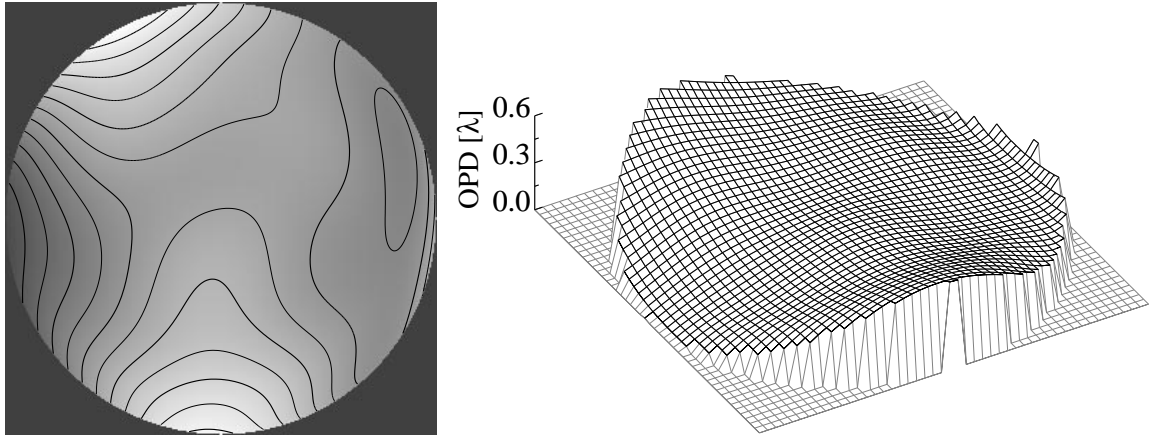


**Figure 3.** Sub-aperture A. Contour and surface plots of the measured wavefront. The contours are separated by 0.05 waves, or  $\lambda/20$ .

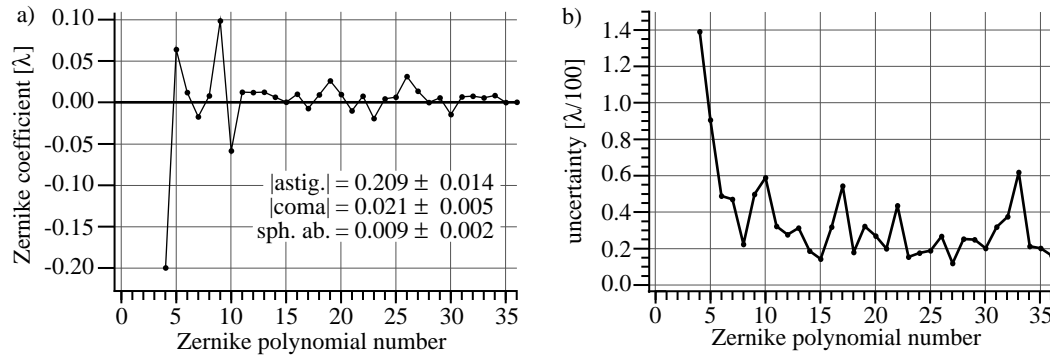


**Figure 4.** Sub-aperture A. (a) Zernike coefficients are based on 19 phase-shifting measurement series, or 114 individual interferograms. (b) The fitting-coefficient uncertainties are based only on the variations of the measured coefficients from the 19 individual measurements.

**Table 1.** Sub-aperture A measured wavefront aberration magnitudes. The Zernike coefficient, P-V, and RMS magnitudes with uncertainties are given for each component.

Sub-aperture A: wavefront statistics						
$\sigma: 0.099 \pm 0.006 \lambda = 1.32 \pm 0.08 \text{ nm} = \lambda/10.1 \pm \lambda/166$						
P-V: $0.593 \pm 0.086 \lambda = 7.94 \pm 1.16 \text{ nm} = \lambda/1.7 \pm \lambda/12$						
aberration	Zernike coefficient		P-V		RMS	
	$[\lambda]$	[nm]	$[\lambda]$	[nm]	$[\lambda]$	[nm]
astigmatism	$0.209 \pm 0.014$	$2.80 \pm 0.19$	$0.418 \pm 0.028$	$5.60 \pm 0.38$	$0.085 \pm 0.006$	$1.14 \pm 0.08$
coma	$0.021 \pm 0.005$	$0.28 \pm 0.07$	$0.042 \pm 0.01$	$0.56 \pm 0.13$	$0.007 \pm 0.002$	$0.09 \pm 0.03$
spherical aberration	$0.009 \pm 0.002$	$0.12 \pm 0.027$	$0.018 \pm 0.004$	$0.24 \pm 0.05$	$0.004 \pm 0.001$	$0.05 \pm 0.01$

are calculated for each phase-shifting data set. Comparison and combination of separate measurements are performed using the wavefronts reconstructed from these Zernike coefficients. In this way, spurious mid- and high-spatial-frequency contributions are removed.

#### 7.2.4 Sub-Aperture A

Sub-aperture A is considered to be the most important sub-aperture of the 10 $\times$  Schwarzschild objective. Based on the results of visible light interferometry, performed by Tim Gleason at Telandic, this 0.07 NA sub-aperture was predicted to have nearly diffraction-limited performance.

Nineteen separate phase-shifting measurements, or 114 individual interferogram exposures, are combined to form the wavefront phasemaps shown in Fig. 3. All of these measurements are from the “downstream” field point, using pinholes A and B. The average of twelve measurements from pinhole A are combined with the average of nine measurements from pinhole B to remove the geometric coma systematic error.

The wavefront phasemaps shown in Fig. 3 are generated from the first 37 Zernike polynomials shown

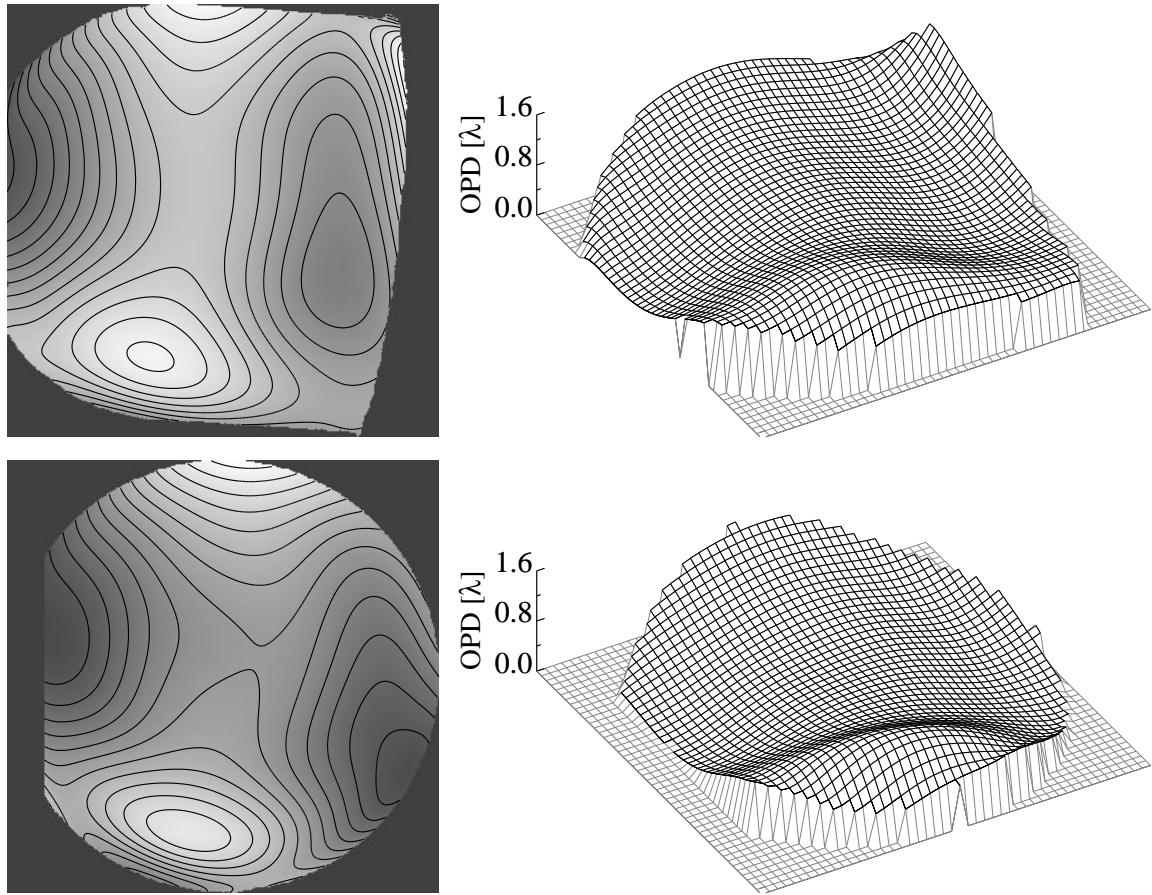


**Figure 5.** Sub-aperture B. Contour and surface plots of the measured wavefront. (Above) The wavefront over the whole “D”-shaped aperture. (Below) Measurements over a circular sub-region of the full aperture, excluding the inner-most portion. The contours are separated by 0.1 waves, or  $\lambda/10$ .

in Fig. 4(a). The position-dependent piston, tilt, and defocus components are removed from the analysis. Table 1 shows the aberration magnitudes and measurement uncertainties for the low-ordered aberration components. Here, astigmatism is the dominant aberration component, with 0.418 waves P-V, or 0.085 waves RMS.

Qualitative verification of the measured aberrations comes from the imaging experiments performed with this sub-aperture. These experiments are described in Section 7.3.

### 7.2.5 Sub-Aperture B

Sub-aperture B was designed to have a 0.08 NA circular pupil, but the pupil-defining aperture was broken during fabrication and the pupil shape became a “D” facing away from the optic axis of the Schwarzschild objective. Unfortunately, near the outer edge of the aperture, in the area designed to be blocked by the aperture, the wavefront has a high degree of curvature in one direction. This curvature significantly complicates interferometric measurement of this sub-aperture.

PS/PDI measurements require that the aberrations be small enough that the test and reference beams are well-separable given the fixed image-plane spacing between the reference pinhole and the window. Where aberrations are large, this separation distance must be increased. Although the 4.5- $\mu\text{m}$  center-to-center spacing of the reference pinhole and window is adequate for the measurement of the other sub-apertures, here it is too narrow. The high curvature of the wavefront along one direction certainly elongates the focal spot in that direction. Since the measurements are performed in two orientations of the beam separation, the problems are limited to the one orientation in which the beam separation is parallel to the beam elongation: this is where the overlap is most severe. In the orthogonal orientation, the overlap is not an impediment to measurement.

Due to a misalignment of the CCD detector, interferometric data is not available for the innermost portion of the aperture. From the available data, two wavefront surfaces are presented in Fig. 5. The upper surface represents the measured

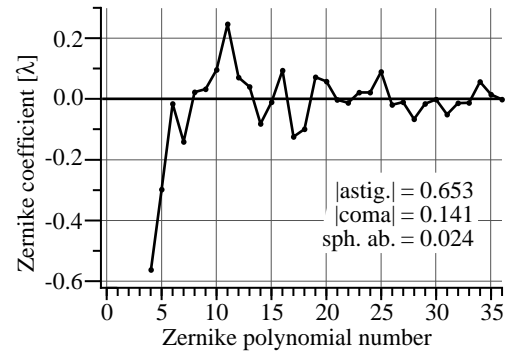


**Figure 6.** Sub-aperture B. Zernike coefficients based on 9 individual interferograms are reported for a circular sub-region of the “D”-shaped aperture.

**Table 2.** Sub-aperture B measured wavefront aberration magnitudes.

#### Sub-aperture B: wavefront statistics for the full aperture

$\sigma$ :	0.260 $\lambda$	=	3.49 nm	=	$\sim\lambda/3.8$
P-V:	1.392 $\lambda$	=	18.65 nm	=	$\sim 7\lambda/5$

#### Sub-aperture B: wavefront statistics for the circular sub-aperture

$\sigma$ :	0.290 $\lambda$	=	3.88 nm	=	$\sim\lambda/3.4$
P-V:	1.344 $\lambda$	=	18.01 nm	=	$\sim 4\lambda/3$

aberration	Zernike coefficient		P-V		RMS	
	[ $\lambda$ ]	[nm]	[ $\lambda$ ]	[nm]	[ $\lambda$ ]	[nm]
astigmatism	0.635	8.51	1.270	17.02	0.259	3.47
coma	0.141	1.89	0.282	3.78	0.050	0.67
spherical aberration	0.024	0.32	0.048	0.64	0.011	0.14

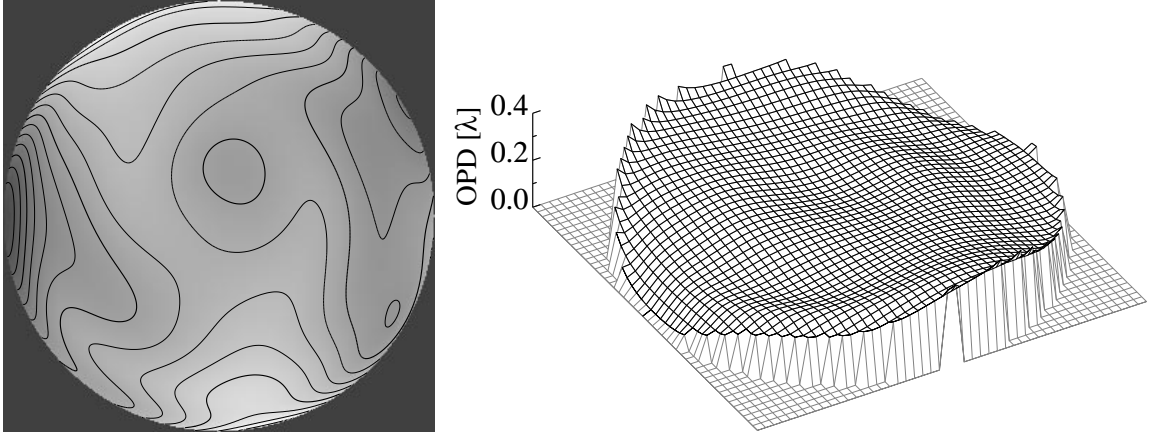


**Figure 7.** Sub-aperture C. Contour and surface plots of the measured wavefront. The contours are separated by 0.025 waves, or  $\lambda/40$ .

wavefront across the entire “D”-shaped pupil. The lower surface imposes a circular sub-region on the measured domain to approximate the wavefront characteristics that would have been observed if the aperture had not been broken.

Wavefront statistics for the circular sub-region are shown in Table 2, based on the Zernike coefficients shown in Fig. 6. No error estimate is given for the Zernike coefficients presented here because only one pair of phase-shifting data series (10 interferograms) was combined to compute the wavefront.

### 7.2.6 Sub-Aperture C

The third and smallest sub-aperture, designed for 0.06 NA, was found to have the smallest wavefront aberrations of the three sub-apertures tested. The wavefront aberrations are smaller than over any other equivalent 0.06 NA region of the other two sub-apertures. Figure 7 shows the wavefront phasemap. The wavefront statistics are given in Table 3, and the Zernike polynomial coefficients are shown in Fig. 8. Again, no error estimate is given for the Zernike coefficients because only one pair of phase-shifting data series (10 interferograms) was combined to compute the wavefront.

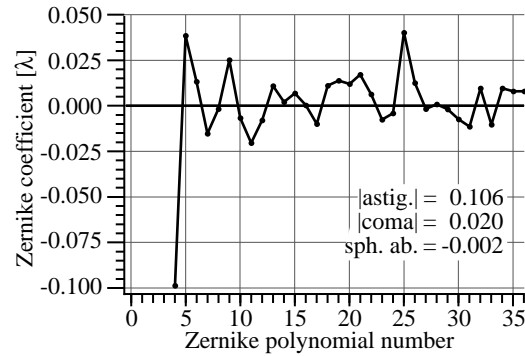


**Figure 8.** Sub-aperture C. Zernike coefficients are based on 10 individual interferograms in two phase-shifting series.

**Table 3.** Sub-aperture C measured wavefront aberration magnitudes.

Sub-aperture C: wavefront statistics						
$\sigma$ : 0.048 $\lambda$ = 0.64 nm = $\sim\lambda/21$						
P-V: 0.367 $\lambda$ = 4.92 nm = $\sim\lambda/2.7$						
aberration	Zernike coefficient		P-V		RMS	
	[ $\lambda$ ]	[nm]	[ $\lambda$ ]	[nm]	[ $\lambda$ ]	[nm]
astigmatism	0.106	1.42	0.212	2.84	0.043	0.58
coma	0.020	0.27	0.041	0.54	0.007	0.10
spherical aberration	-0.002	-0.02	-0.003	-0.04	-0.001	-0.01



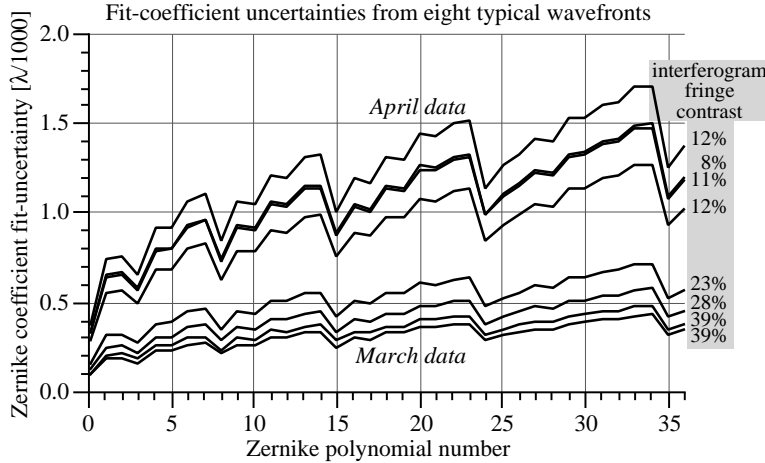


**Figure 9.** Uncertainties in the wavefront surface fit coefficients are shown for eight typical phase-shifting measurements of sub-aperture A. The uncertainties are based on the fit variance, as described in Section 15.6. The qualitative difference between the March and April measurements is related to an overall decrease in the fringe contrast observed in the April measurements. The fringe contrast in the corresponding interferograms is shown next to each set of uncertainties. The relationship between fringe contrast and coefficient uncertainty is investigated in Section 8.11.

### 7.2.7 Measurement Precision

Estimation of the wavefront measurement precision is performed on several fronts; this is the primary subject of Chapter 8. Experimentally, the dominant effect is the measurement-to-measurement variation that is observed in the wavefront fitting data. The other contribution to the uncertainty comes from the fit-variances related to noise in the raw data. Because there are so many data points under consideration and the data is of relatively high quality after localized blemishes are removed, the contributions from the fit-variances are *significantly* smaller than from the former effect.

Only sub-aperture A was measured a sufficient number of times for an ensemble of measurements to be compiled. The standard deviation for each individual Zernike polynomial coefficient of the measurements made of this sub-aperture is plotted in Fig. 4(b) (Section 7.2.4). With a magnitude of 0.014 waves (0.188 nm, or  $\sim\lambda/70$ ), the uncertainty is largest in one of the two astigmatism coefficients. For the others, the typical uncertainty values are roughly 0.003 waves (0.040 nm, or  $\sim\lambda/300$ ).

The less significant contribution to the uncertainties is that associated with the fit-variance, as described in Section 15.6. Here the uncertainties are related to the quality of the fit, dependent essentially on the mid- and high-spatial-frequency noise in the data. As each individual phase-shifting data series is analyzed and the wavefront surface fitting is performed, the uncertainty in each coefficient is calculated.

The coefficient uncertainties for eight typical phase-shifting series from the measurement of sub-aperture A are shown in Fig. 9. There is a clear distinction in the magnitudes of the coefficient uncertainties between the March and April data sets. These two separate sets of measurements are described in Section 8.6. Experimental evidence suggests that the discrepancy is strongly dependent on differences in the observed interferogram fringe contrasts. This point is investigated further in Section 8.11. Only data from the March data sets were used to compile the sub-aperture A phasemap shown in this chapter. For these measurements the *largest* coefficient uncertainty is below  $7.5 \times 10^{-4}$  waves (0.010 nm, or  $\sim\lambda/1300$ ).

Thus it is clear that the contribution from the fitting uncertainty is *much* less than from the measurement-to-measurement variation. It is important to note here that although the fitting uncertainty in the April data is more than twice as large as in the March data, the measured wavefront difference between the two data sets is only 0.018 waves RMS (0.241 nm, or  $\sim\lambda/57$ ) and the differences in the measured Zernike coefficients have a typical value below 0.005 waves (0.067 nm, or  $\lambda/200$ ) (Section 6.6.2).

### 7.2.8 Zonal Fabrication Error

The presence of astigmatism as the dominant term in each measured sub-aperture suggests a trend characteristic of this annular Schwarzschild objective as a whole. As the system is aligned for the measurement of each sub-aperture, the reference pinhole is placed in the position that produces the best fringe contrast in the interferogram. For an astigmatic wavefront, characterized by a *cylindrically-shaped* aberration, this is the position that *balances* the defocus components in the two orthogonal directions of the astigmatism. Adding a small amount of defocus to the measured wavefront is equivalent to a longitudinal translation of the reference pinhole, placing it closer to the *best focus* in one of the two directions (i.e. the *tangential* or *sagittal* focus).

Figure 10(a) shows the three measured wavefronts rotated into their proper orientation and placed in position within the three-aperture pupil. By adding a small amount of defocus to each measured wavefront and observing the resulting annular pattern, shown in Fig. 10(b), it is possible to argue that the astigmatism measured in each sub-aperture comes from an overall *zonal error* in the optical system. This small error, of magnitude less than  $\lambda/2$ , or  $\sim 7$  nm, could be a figure error in either of the optical substrates, or could be related to multilayer thickness variations. Verification of an overall zonal error can only be made

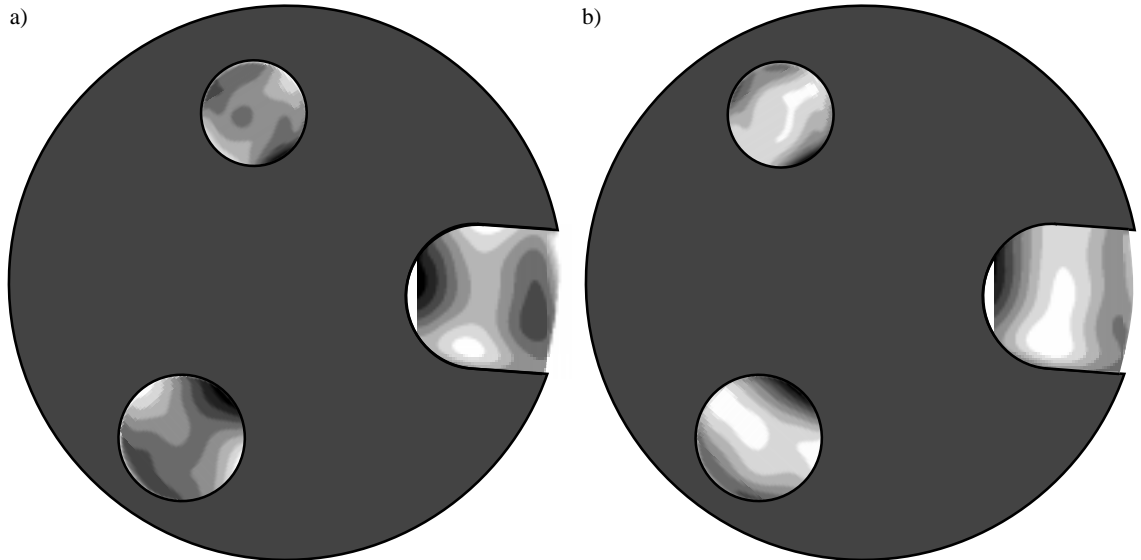


**Figure 10.** (a) Measured wavefront phasemaps of the three sub-apertures of the 10 $\times$  Schwarzschild objective oriented and positioned within the pupil-defining aperture. (b) Adding a small amount of defocus to the measured astigmatic phasemaps reveals the possibility of a zonal fabrication error in the annular optic.

by the simultaneous measurement of all three sub-apertures, or by measurements made with very close attention to the absolute coordinates of the reference pinhole. Neither is possible at this point, so the existence of a zonal error can be no more than a reasonable conjecture.

It is much more likely that a zonal error would be caused by an error in the substrate figure than by the multilayers, since any changes in the multilayer thickness capable of producing a  $\lambda/2$  phase variation would most likely be accompanied by a loss in reflectivity. Such reflectivity changes are not observed. Furthermore, the multilayer thicknesses were measured after deposition and were observed to meet the design specifications. The substrate figure may not have been measured with an accuracy high enough to observe fabrication errors of this small size.

### 7.3 IMAGING EXPERIMENTS

At the conclusion of the interferometric measurements, the 10× Schwarzschild objective was brought to Sandia National Laboratory, in Livermore, California, to perform imaging experiments using the 10×I EUV imaging system (Tichenor et al. 1993, 1994), shown schematically in Fig. 11. The “10×I” Schwarzschild objective designed to be used in the Sandia system shares the same optical design as the Berkeley “10×B”, and the mechanical housings are similar enough that installation of 10×B in the Sandia system is trivial.

The Sandia system uses a laser-produced plasma source. Light is collected by an ellipsoidal condenser and directed toward the reflective EUV test-pattern mask with a near-45° turning mirror. The system uses Köhler-type illumination with a partial coherence factor near 0.5. As with the interferometry experiments, here too the Schwarzschild objective is oriented vertically and is illuminated from below. A photoresist-coated wafer rests on the three-ball mount at the top of the optic and records the image of the mask. A manually-adjusted translation stage literally pushes the wafer forward in one direction, allowing multiple exposures to be made on a single wafer.

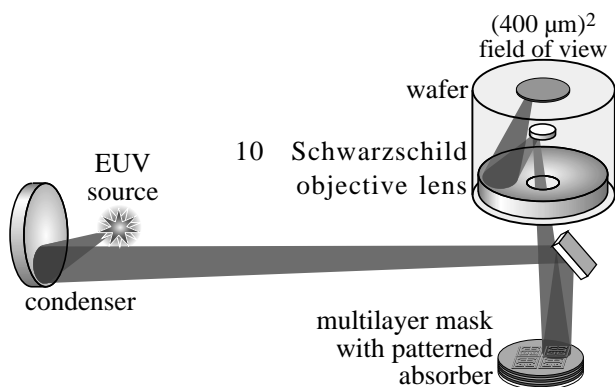


**Figure 11.** A schematic representation of the key components of the Sandia 10×I EUV imaging system. The system utilizes a laser-plasma source and reflective multilayer-coated optics to illuminate the mask which is patterned on a reflective multilayer-coated substrate. A 10×-demagnification Schwarzschild objective (such as the 10×B, Berkeley objective) is used to project an image of the mask onto a photoresist-coated wafer that rests on a three-ball mount at the top of the objective. The longitudinal (vertical) position of the mask may be adjusted to bring the image of the mask into focus on the wafer. The 10×B objective was brought to Sandia to perform imaging experiments using this system.

### 7.3.1 Experimental Results and Predicted Behavior

Comparison of the recorded results with the predicted performance shows very good agreement. The results of imaging experiments at the resolution limit of the system are presented in this section.

The choice of the negative-tone, chemically-amplified resist SAL 601 was a compromise between sensitivity and resolution. With 100-nm-thick resist the images appear grainy, but the essential features are clearly visible in SEM micrographs. Figure 12 shows a line-and-space pattern of 0.2- $\mu\text{m}$  pitch, where the smallest individual features are 0.1- $\mu\text{m}$  wide.

The performance of the system and the predictive powers of the interferometry are more clearly revealed in images of an *Archimedes star* test pattern, shown in Fig. 13. On a single wafer, images were recorded at multiple focal positions, with a 1- $\mu\text{m}$  increment. Focal adjustments were actually performed by longitudinal translation of the mask in 100- $\mu\text{m}$  steps, which is nearly equivalent to a 1- $\mu\text{m}$  longitudinal translation of the image plane, with a very slight change in the magnification (power).

Sub-aperture A was the only aperture used for these imaging experiments. The wavefront aberrations in this sub-aperture are dominated by astigmatism of 0.418 waves P-V, or 0.085 waves RMS. Astigmatism causes the focusing properties to be different along two orthogonal directions. The primary characteristic of an optical system containing astigmatic aberrations is that the longitudinal positions of best-focusing occur at separate planes for the two directions of the astigmatism. In other words, horizontal and vertical features (for example) form their sharpest images in different planes. This effect is clearly observable in the SEM micrographs of Fig. 13. Here, when the system is a few microns out of focus, the sharpness of the thinnest features is noticeably different in the horizontal and vertical directions. On opposite sides of focus, the two directions reverse roles. The asymmetry of these features in passing through focus can be attributed to an

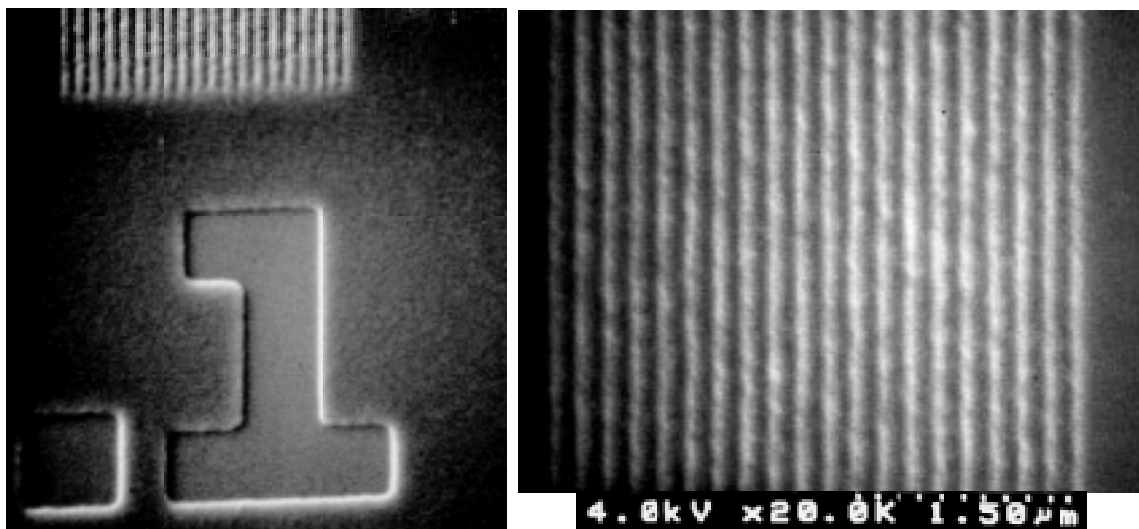


**Figure 12.** SEM micrographs of a resolution test pattern exposed in SAL 601 photoresist. The pattern is of 0.1- $\mu\text{m}$  lines and spaces. The image on the right is a detail of the region at the top of the image on the left.

unintended difference in the exposure dose.

Based on the measured wavefront at 0.07 NA, an illumination partial coherence factor of 0.5, and 13.4-nm wavelength, detailed calculations were performed to predict the imaging behavior of 10×B (Tejnil et al. 1997) with the Archimedes star resolution test image. These calculations were performed using the SPLAT imaging simulation program developed at the University of California, Berkeley. The simulation yields the predicted field amplitude in the wafer plane. Adjacent to each exposure measurement, Fig. 13 shows several predictions of the imaging quality based on the application of simple threshold values to the predicted field intensity. With a unit intensity bright-field image, the thresholds are intended to simulate the behavior of the resist. Given the limitations of the resist material and the uncertainties in the exposure and development processes, comparison of the simulations with the SEM micrographs shows excellent agreement.

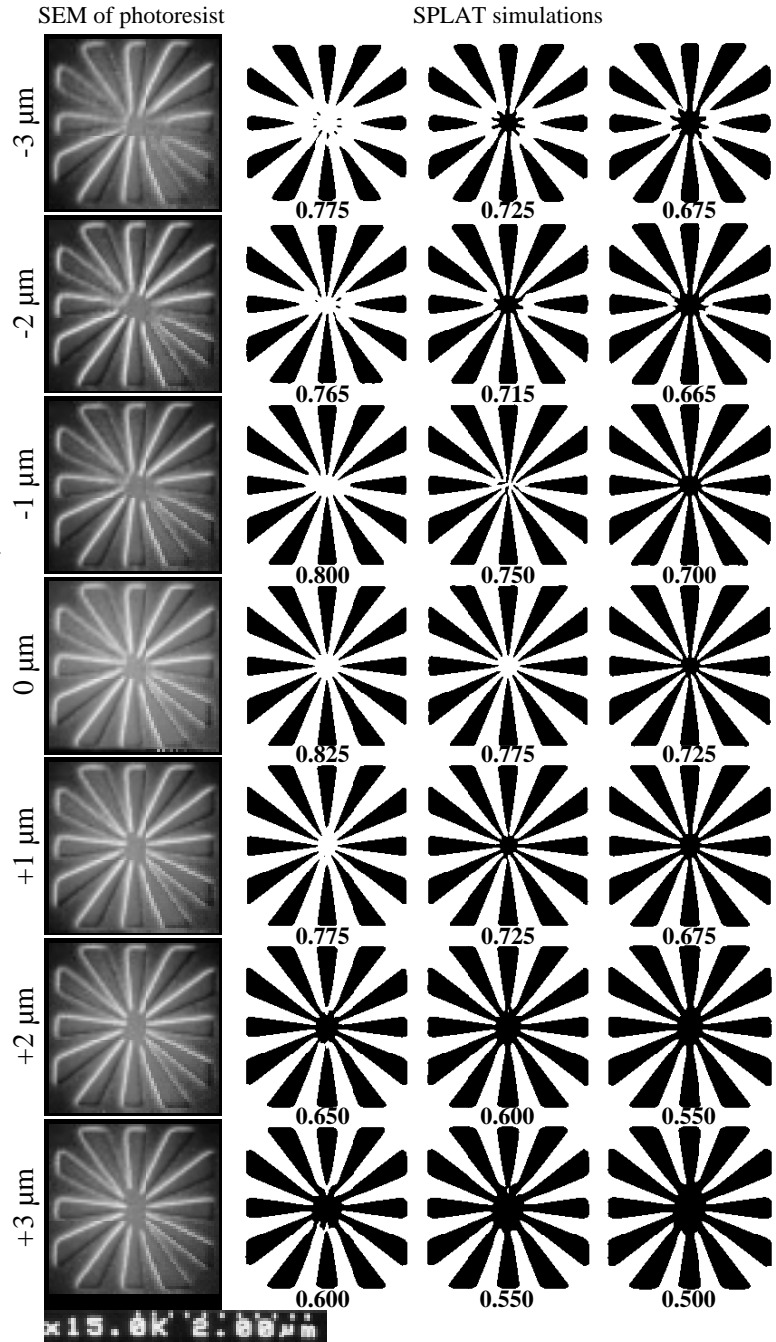


**Figure 13.** (Left column) SEM micrographs of an *Archimedes star* resolution test pattern, measured at seven positions through-focus. The amount of defocus is indicated at the left of each image. The characteristics of the astigmatic wavefront are clearly observable in the pattern: the horizontal features are sharpest when the system is defocused by 3 μm in the *negative* direction, while the vertical features are sharpest at 3 μm in the *positive* direction. Simulations of the imaging properties are shown to the right of each image. A simple threshold is applied at three levels to the predicted field intensity to model the behavior of the photoresist with different exposure doses. Based on a unit intensity bright field, the threshold values are shown below each simulation image. The qualitative agreement between the predictions and measurements is very good.